

SUPER-LUMINOUS TYPE Ic SUPERNOVAE: CATCHING A MAGNETAR BY THE TAIL

C. INSERRA¹, S. J. SMART¹, A. JERKSTRAND¹, S. VALENTI^{2,3}, M. FRASER¹, D. WRIGHT¹, K. SMITH¹, T.-W. CHEN¹, R. KOTAK¹,
A. PASTORELLO⁴, M. NICHOLL¹, F. BRESOLIN⁵, R. P. KUDRITZKI⁵, S. BENETTI⁴, M. T. BOTTICELLA⁶, W. S. BURGETT⁵,
K. C. CHAMBERS⁵, M. ERGON⁷, H. FLEWELLING⁵, J. P. U. FYNBO⁸, S. GEIER^{8,9}, K. W. HODAPP⁵, D. A. HOWELL^{2,3}, M. HUBER⁵,
N. KAISER⁵, G. LELOUDAS^{8,10}, L. MAGILL¹, E. A. MAGNIER⁵, M. G. MCCRUM¹, N. METCALFE¹¹, P. A. PRICE⁵, A. REST¹²,
J. SOLLERMAN⁷, W. SWEENEY⁵, F. TADDIA⁷, S. TAUBENBERGER¹³, J. L. TONRY⁵, R. J. WAINSCOT⁵, C. WATERS⁵, AND D. YOUNG¹

¹ Astrophysics Research Centre, School of Mathematics and Physics, Queens University Belfast, Belfast BT7 1NN, UK; c.inserra@qub.ac.uk

² Las Cumbres Observatory Global Telescope Network, 6740 Cortona Dr., Suite 102 Goleta, CA 93117, USA

³ Department of Physics, University of California, Santa Barbara, Broida Hall, Mail Code 9530, Santa Barbara, CA 93106-9530, USA

⁴ INAF, Osservatorio Astronomico di Padova, vicolo dell'Osservatorio 5, I-35122 Padova, Italy

⁵ Institute of Astronomy, University of Hawaii, 2680 Woodlawn Drive, Honolulu, HI 96822, USA

⁶ INAF-Osservatorio Astronomico di Capodimonte, Salita Moiariello 16, I-80131 Napoli, Italy

⁷ The Oskar Klein Centre, Department of Astronomy, AlbaNova, Stockholm University, SE-10691 Stockholm, Sweden

⁸ Dark Cosmology Centre, Niels Bohr Institute, University of Copenhagen, DK-2100 Copenhagen, Denmark

⁹ Nordic Optical Telescope, Apartado 474, E-38700 Santa Cruz de La Palma, Spain

¹⁰ The Oskar Klein Centre, Department of Physics, Stockholm University, SE-10691 Stockholm, Sweden

¹¹ Department of Physics, Durham University, South Road, Durham DH1 3LE, UK

¹² Space Telescope Science Institute, 3700 San Martin Drive, Baltimore, MD 21218, USA

¹³ Max-Planck-Institut für Astrophysik, Karl-Schwarzschild-Str. 1, D-85741 Garching, Germany

Received 2013 April 11; accepted 2013 April 30; published 2013 June 4

ABSTRACT

We report extensive observational data for five of the lowest redshift Super-Luminous Type Ic Supernovae (SL-SNe Ic) discovered to date, namely, PTF10hgi, SN2011ke, PTF11rks, SN2011kf, and SN2012il. Photometric imaging of the transients at +50 to +230 days after peak combined with host galaxy subtraction reveals a luminous tail phase for four of these SL-SNe. A high-resolution, optical, and near-infrared spectrum from *xshooter* provides detection of a broad He I $\lambda 10830$ emission line in the spectrum (+50 days) of SN2012il, revealing that at least some SL-SNe Ic are not completely helium-free. At first sight, the tail luminosity decline rates that we measure are consistent with the radioactive decay of ^{56}Co , and would require 1–4 M_{\odot} of ^{56}Ni to produce the luminosity. These ^{56}Ni masses cannot be made consistent with the short diffusion times at peak, and indeed are insufficient to power the peak luminosity. We instead favor energy deposition by newborn magnetars as the power source for these objects. A semi-analytical diffusion model with energy input from the spin-down of a magnetar reproduces the extensive light curve data well. The model predictions of ejecta velocities and temperatures which are required are in reasonable agreement with those determined from our observations. We derive magnetar energies of $0.4 \lesssim E(10^{51} \text{ erg}) \lesssim 6.9$ and ejecta masses of $2.3 \lesssim M_{\text{ej}}(M_{\odot}) \lesssim 8.6$. The sample of five SL-SNe Ic presented here, combined with SN 2010gx—the best sampled SL-SNe Ic so far—points toward an explosion driven by a magnetar as a viable explanation for all SL-SNe Ic.

Key words: stars: magnetars – supernovae: general – supernovae: individual (PTF10hgi, PTF11rks, SN 2011ke, SN 2011kf, SN 2012il)

Online-only material: color figures

1. INTRODUCTION

The discovery of unusually luminous optical transients by modern supernova (SN) surveys has dramatically expanded the observational and physical parameter space of known SN types. The Texas Supernova Search was a pioneer in this area, with one of the first searches of the local universe without a galaxy bias (Quimby et al. 2005). This has been followed by deeper, wider surveys from the Palomar Transient Factory (PTF; Rau et al. 2009), the Panoramic Survey Telescope and Rapid Response System (Pan-STARRS; Kaiser et al. 2010), the Catalina Real-time Transient Survey (CRTS; Drake et al. 2009), and the La Silla QUEST survey (Hadjiyska et al. 2012), all of which have found unusually luminous transients which tend to be hosted in intrinsically faint galaxies. These Super-Luminous SNe (SL-SNe) show absolute magnitudes at maximum light of $M_{\text{AB}} < -21$ mag and total radiated energies of the order of 10^{51} erg. They are factors of 5–100 brighter than Type Ia SNe or normal core-collapse events. Gal-Yam (2012) proposed that three distinct physical groups of SL-SNe have emerged. The

first group which was recognized was the luminous Type II SNe epitomized by SN 2006gy (Smith et al. 2007; Smith & McCray 2007; Ofek et al. 2007; Agnoletto et al. 2009), which show signs of strong circumstellar interaction. The second group includes Type Ic SNe that have broad, bright light curves and decay rates that imply that they could be due to pair-instability explosions powered by large ejecta masses of ^{56}Ni (3–5 M_{\odot}). To date only one object of this type (SN 2007bi) has been published and studied in detail (Gal-Yam et al. 2009; Young et al. 2010). The third group was labeled by Gal-Yam (2012) as Super-Luminous Type I SNe (SL-SNe I) and the two earliest examples are SCP-06F6 and SN 2005ap (Barbary et al. 2009; Quimby et al. 2007), which are characterized at early times by a blue continuum and a distinctive “W”-shaped spectral feature at ~ 4200 Å. In this paper we will call this type Super-Luminous Type Ic SNe (or SL-SNe Ic), simply because they are Type Ic in the established SN nomenclature and are extremely luminous.

The existence of this class of SL-SNe Ic was firmly established when secure redshifts were determined with the identifi-

cation of narrow Mg II $\lambda\lambda 2796, 2803$ absorption from the host galaxies in the optical spectra of $z > 0.2$ transients by Quimby et al. (2011b). The spectra of four PTF transients, SCP-06F6, and SN 2005ap were then all linked together with these redshifts establishing a common type (Quimby et al. 2011b). Subsequently, the identification of host galaxy emission lines such as [O II] $\lambda 3727$, [O III] $\lambda\lambda 1959, 5007$, H α , and H β has confirmed the redshift derived from the Mg II absorption in many SL-SNe Ic, such as in the case of SN 2010gx (Quimby et al. 2010; Mahabal & Drake 2010; Pastorello et al. 2010). These distances imply an incredible luminosity with u - and g -band absolute magnitudes reaching about -22 . This luminosity allowed these SNe to be easily identified in the Pan-STARRS Medium Deep fields at $z \sim 1$ (Chomiuk et al. 2011) and beyond (Berger et al. 2012).

The typical spectroscopic signature of the class of SL-SNe Ic is a blue continuum with broad absorption lines of intermediate-mass elements such as C, O, Si, Mg with velocities $10,000 \text{ km s}^{-1} < v < 20,000 \text{ km s}^{-1}$. No clear evidence of H or He has been found so far in the spectra of SL-SNe Ic, whereas Fe, Mg, and Si lines are typically prominent after maximum. The study of the well-sampled SN 2010gx (Pastorello et al. 2010) showed an unexpected transformation from an SL-SN Ic spectrum to that of a normal Type Ic SN. A similar transformation was also observed in the late-time spectrum of PTF09cnd (Quimby et al. 2011b), which evolved to become consistent with a slowly evolving Type Ic SN.

The SL-SNe Ic discovered to date appear to be associated with faint and metal-poor galaxies at redshifts ranging between 0.23 and 1.19 (typically $M_g > -17$ mag; Quimby et al. 2011b; Neill et al. 2011; Chomiuk et al. 2011; Chen et al. 2013), although the highest redshift SL-SNe Ic (PS1-12bam, $z = 1.566$) is in a galaxy which is more luminous and more massive than the lower redshift counterparts (Berger et al. 2012). An estimate of the metallicity of the faint host galaxy of SN 2010gx, from the detection of the auroral [O III] $\lambda 4363$ line, indicates a very low metallicity of $0.05 Z_\odot$ (Chen et al. 2013). Research on SL-SNe Ic is progressing rapidly, with 13 of these intriguing transients now identified since the discovery of SCP-06F6. To power the enormous peak luminosity of SL-SNe Ic with radioactive decay would require several solar masses of ^{56}Ni . However, this is inconsistent with the width of the light curves as shown by Chomiuk et al. (2011). The light curves cannot be reproduced with a physical model that has an ejecta mass significantly greater than the ^{56}Ni mass needed to power the peak. In the case of SN 2010gx, Chen et al. (2013) showed that the tail phase faded to levels which would imply an upper limit of around $0.4 M_\odot$ of ^{56}Ni . Among the scenarios proposed to explain the remarkable peak luminosity are the spin down of a rapidly rotating young magnetar (Kasen & Bildsten 2010; Woosley 2010) that provides an additional reservoir of energy for the SN (Ostriker & Gunn 1971; Usov 1992; Wheeler et al. 2000; Thompson et al. 2004); the interaction of the SN ejecta with a massive ($3\text{--}5 M_\odot$) C/O-rich circumstellar medium (CSM; Blinnikov & Sorokina 2010) or with a dense wind (Chevalier & Irwin 2011; Ginzburg & Balberg 2012); or collisions between high-velocity shells ejected by a pulsational pair instability, which would give rise to successive bright optical transients (Woosley et al. 2007). One of these SNe (SN 2006oz) was discovered 29 days before peak luminosity and showed a flat plateau in the rest-frame NUV before its rise to maximum, indicating that finding these objects early could give constraints on the explosion channel (Leloudas et al. 2012).

In most cases to date, however (apart from SN 2010gx; Chen et al. 2013), the lightcurves and energy released at >100 d is unexplored territory. Chen et al. (2013) quantified the host of SN 2010gx, but difference imaging showed no detection of SN flux at 250–300 days to deep limits. Quimby et al. (2011a) detected flux at the position of PTF09cnd at +138 d after peak in a B -band image, but it is not clear if this flux is from the host or the SN. In this paper we present the detailed follow-up of five SL-SNe Ic at $0.100 < z < 0.245$, namely, PTF11rks, SN 2011ke, SN 2012il, PTF10hgi, and SN 2011kf, and attempt to follow them for as long as possible to garner further evidence to probe the physical mechanism powering these intriguing events. A detailed analysis of their hosts will be part of a future paper (T.-W. Chen et al., in preparation).

This paper is organized as follows. In Section 2 we introduce the SNe, and report distances and reddening values. Photometric data, light and color curves, as well as the absolute light curves in the rest frame are presented in Section 3. Section 4 is devoted to the analysis of bolometric and pseudo-bolometric light curves and the evaluation of possible ejected ^{56}Ni masses, while in Section 5 we describe and analyze the spectra. Finally, a discussion about the origin of these transients is presented in Section 6, followed by a short summary in Section 7.

2. DISCOVERY AND TARGET SAMPLE

2.1. Pan-STARRS1 Data: Discovery and Recovery of the Transients

The strong tendency for these SL-SNe to be hosted in faint galaxies appears not to be a bias, which suggests a straightforward way of finding them in large volume, wide-field searches. With the Pan-STARRS1 survey, we have been running the ‘‘Faint Galaxy Supernova Survey’’ (FGSS) which is aimed at finding transients in faint galaxies originally identified in the Sloan Digital Sky Survey (SDSS) catalog (Valenti et al. 2010).

The Pan-STARRS1 optical system uses a 1.8 m diameter aspheric primary mirror, a strongly aspheric 0.9 m secondary and three-lens corrector and has 8 m focal length (Hodapp et al. 2004). The telescope illuminates a diameter of 3.3 deg and the ‘‘GigaPixel Camera’’ (Tonry & Onaka 2009) comprises a total of 60 4800×4800 pixel detectors, with $10 \mu\text{m}$ pixels that subtend 0.258 arcsec (for more details, see Magnier et al. 2013). The PS1 filter system is described in Tonry et al. (2012b), and is similar to but not identical to the SDSS *griz* (York et al. 2000) filter system. However, it is close enough that cataloged cross-matching between the surveys can identify high amplitude transients. In this paper, we will convert all the PS1 filter magnitudes $g_{P1} r_{P1} i_{P1} z_{P1} y_{P1}$ to the SDSS AB magnitude system as the bulk of the follow-up data were taken in SDSS-like filters (see Section 3 for more details).

The PS1 telescope is operated by the PS1 Science Consortium (PS1SC) to undertake several surveys, with the two major ones being the ‘‘Medium Deep Field’’ survey (e.g., Botticella et al. 2010; Tonry et al. 2012a; Gezari et al. 2012; Berger et al. 2012) which was optimized for transients (allocated around 25% of the total telescope time) and the wide-area 3π survey, allocated around 56% of the available observing time. As described in Magnier et al. (2013), the goal of the 3π survey is to observe the portion of the sky north of -30 deg declination, with a total of 20 exposures per year across all five filters for each field center. The 3π survey plan is to observe each field center four times in each of $g_{P1} r_{P1} i_{P1} z_{P1} y_{P1}$ during a 12 month period, although this can

be interrupted by bad weather. As described by Magnier et al. (2013), the four epochs in a calendar year are typically split into two pairs called Transient Time Interval (TTI) pairs which are single observations separated by 20–30 minutes to allow for the discovery of moving objects. The temporal distribution of the two sets of TTI pairs is not a well-defined and straightforward schedule. The blue bands (g_{P1} , r_{P1} , i_{P1}) are scheduled close to opposition to enhance asteroid discovery with g_{P1} and r_{P1} being constrained in dark time as far as possible. The z_{P1} and y_{P1} filters are scheduled far opposition to optimize for parallax measurements of faint red objects. Although a large area of sky is observed each night (typically 6000 deg²), the moving object and parallax constraints mean the 3π survey is not optimized for finding young, extragalactic transients in a way that the PTF and La Silla-QUEST projects are. The exposure times at each epoch (i.e., in each of the TTI exposures) are 43 s, 40 s, 45 s, 30 s, and 30 s in $g_{P1}r_{P1}i_{P1}z_{P1}y_{P1}$. These reach typical 5σ depths of roughly 22.0, 21.6, 21.7, 21.4, and 19.3 as estimated from point sources with uncertainties of 0^m.2 (in the PS1 AB magnitude system described by Tonry et al. 2012b).

The PS1 images are processed by the Pan-STARRS1 Image Processing Pipeline (IPP), which performs automatic bias subtraction, flat fielding, astrometry (Magnier et al. 2008), and photometry (Magnier 2007). These photometrically and astrometrically calibrated catalogs produced in MHPCC are made available to the PS1SC on a nightly basis and are immediately ingested into a MySQL database at Queen’s University Belfast. We apply a tested rejection algorithm and cross match the PS1 objects with SDSS objects in the DR7 catalog¹⁴ (Abazajian et al. 2009). We apply the following selection filters to the PS1 data (all criteria must be simultaneously fulfilled).

1. PS1 source must have $15 < g_{P1} < 20$ or $15 < r_{P1} < 20$ or $15 < i_{P1} < 20$ or $15 < z_{P1} < 20$.
2. SDSS counterpart must have $18 < r_{SDSS} < 23$.
3. Distance between PS1 source and SDSS source must be < 3 arcsec.
4. PS1 mag must be 1.5 mag brighter than SDSS (in the corresponding filter).
5. The PS1 object must be present in both TTI pairs and the astrometric recurrences be $< 0''.3$. Objects with multiple detections must have rms scatter $< 0''.1$.
6. The PS1 object must not be in the galactic plane ($|b| > 5^\circ$).

All objects are then displayed through a Django-based interface to a set of interactive Web sites, and human eyeballing and checking takes place. We use the star–galaxy separation in SDSS to guide us in what may be variable stars (i.e., stellar sources in SDSS which increase their luminosity) or extragalactic transients (i.e., quasi-stellar objects (QSOs), active galactic nuclei (AGNs), and SNe). While the cadence of the PS1 observations is not ideal for detections of young SNe we have found many SNe in intrinsically faint galaxies. As of 2013 January, spectroscopically confirmed objects include 34 QSOs or AGNs and 41 SNe. Several of these have been confirmed as SL-SNe. Pastorello et al. (2010) presented the data of SN 2010gx recovered in 3π images, and in many cases the same object is detected by the Catalina Real-Time Transient Survey (CSS/MSS) and PTF. As we are not doing difference imaging and only comparing to objects in the SDSS footprint, there are some cases where objects are reported by PTF or CRTS and interesting pre-discovery epochs are available in PS1. As 3π difference imaging is not

being carried out routinely, we often use the PTF and CRTS announcements to inform a retrospective search. In this paper, we present five SL-SNe Ic which were either detected through the PS1 FGSS, or were announced in the public domain. A sixth object (PTF12dam \equiv PS1-12arh) is discussed in a companion paper (M. Nicholl et al., in preparation). In all five cases follow-up imaging and spectroscopy was carried out as discussed below.

For all the SNe listed here (and throughout this paper) we adopt a standard cosmology with $H_0 = 72$ km s⁻¹, $\Omega_M = 0.27$, and $\Omega_\Lambda = 0.73$. There is no detection of Na I interstellar medium (ISM) features from the host galaxies, nor do we have any evidence of significant extinction in the hosts from the SNe themselves. This suggests that the absorption in host is low and we assume that extinction from the host galaxies is negligible. Although we do detect Mg II ISM lines from the hosts in some cases, there is no clear correlation with these line strengths and line of sight extinction. In all cases only the Milky Way foreground extinction was adopted.

2.2. PTF10hgi

PTF10hgi was first discovered by PTF on 2010 May 15.5 and announced on 2010 July 15 (Quimby et al. 2010). The spectra taken by PTF on May 21.0 UT and June 11.0 UT were reported as a blue continuum with faint features typical of SL-SNe Ic. Another spectrum obtained by PTF on July 7.0 UT was similar to PTF09end at three weeks past peak brightness. Initiated by Quimby et al. (2010), ultraviolet (UV) observations were obtained with *Swift*+UVOT in 2010 July, and we analyze those independently later in Section 3. PTF10hgi lies outside the SDSS DR9¹⁵ area (Ahn et al. 2012), hence was not discovered by our PS1 FGSS software. However, after the announcement (Quimby et al. 2010), we recovered it in PS1 images taken (in band r_{P1}) on 2010 May 18 and on four other epochs around peak magnitude (in bands $g_{P1}r_{P1}i_{P1}$), listed in Table A1.

We detect a faint host galaxy in deep *griz*-band images taken with the William Herschel Telescope on 2012 May 26 and the Telescopio Nazionale Galileo on 2012 May 28. At a magnitude $r = 22.01 \pm 0.07$, this is too faint to affect the measurements of the SN flux up to +90 days. There are no host galaxy emission lines detected in our spectra, hence the redshift is determined through cross-correlation of the spectra of PTF10hgi with other SNe at confirmed redshift indicating a redshift of $z = 0.100 \pm 0.014$, corresponding to a luminosity distance of $d_L \sim 448$ Mpc. The Galactic reddening toward the SN line of sight is $E(B - V) = 0.09$ mag (Schlegel et al. 1998).

2.3. SN 2011ke

SN 2011ke was discovered in the CRTS (CSS110406: 135058+261642) and PTF surveys (PTF11dij) with the earliest detections on 2011 April 6 and March 30, respectively (Drake et al. 2011; Quimby et al. 2011c). We also independently detected this transient in the PS1 FGSS (PS1-11xk) on images taken on 2011 April 15 (Smartt et al. 2011). However, earlier PS1 data show that we can determine the epoch of explosion to around 1 day, at least as far as the sensitivity of the images allow. On MJD 55649.55 (2011 March 29.55 UT) a PS1 image ($r_{P1} = 40$ s) shows no detection of the transient to $r \simeq 21.17$ mag. Quimby et al. (2011c) report the PTF detection on 2011 March 30 (MJD = 55650) the night after the PS1 non-detection at

¹⁴ <http://www.sdss.org/dr7/>

¹⁵ <http://www.sdss3.org/dr9/>

$g \simeq 21$. PS1 detections then occurred one and three days after this on 55651.6 and 55653.6 (in i_{P1} and r_{P1}), respectively. The photometry is given in Table A2. This is the best constraint on the explosion epoch of SL-SNe to date, allowing the rise time and light curve shape to be confidently measured. The object brightened rapidly, by ~ 3 mag in the g band in the first 15 days and 1.7 mag in the subsequent 20 days. It was classified as SL-SNe Ic by both Drake et al. (2011) and Quimby et al. (2011c); their spectra obtained on May 8.0 and 11.0 UT, respectively, showed a blue continuum with faint features, similar to PTF09cnd about one week past maximum light (Quimby et al. 2011c).

We found a nearby source in the SDSS DR9 catalog ($g = 21.10 \pm 0.08$, $r = 20.71 \pm 0.08$), which is the host galaxy as confirmed by deep *griz* images taken with the William Herschel Telescope on 2012 May 26 at a magnitude $g = 21.18 \pm 0.05$, $r = 20.72 \pm 0.04$. The host emission lines set the SN at $z = 0.143$, equivalent to a luminosity distance of $d_L = 660$ Mpc. The Galactic reddening toward the position of the SN is $E(B - V) = 0.01$ mag (Schlegel et al. 1998).

2.4. PTF11rks

PTF11rks was first detected by PTF on 2011 December 21.0 UT (Quimby et al. 2011a). Spectra acquired on December 27.0 UT and 31.0 UT showed a blue continuum with broad features similar to PTF09cnd at maximum light, confirming it as an SL-SN Ic. A non-detection in the r band on December 11 UT prior to discovery is also reported, setting a limit of >20.6 mag at this epoch. Quimby et al. (2011a) detailed a brightening of 0.8 mag in the r band in the first six days after the discovery. Prompt observations with *Swift* revealed a UV source at the optical position of the SN, but no source was detected in X-rays at the same epochs. There are no useful early data from PS1 for this object.

The host galaxy is listed in the SDSS DR9 catalog with $g = 21.59 \pm 0.11$ mag and $r = 20.88 \pm 0.10$ mag. Confirmation of these host magnitudes as achieved with our deep *gr*-band images taken with the William Herschel Telescope on 2012 September 22 at a magnitude $g = 21.67 \pm 0.07$ and $r = 20.83 \pm 0.05$. The emission lines of the host and narrow absorptions consistent with Mg II $\lambda\lambda 2796, 2803$ doublet locate the transient at $z = 0.19$, corresponding to a luminosity distance of $d_L = 904$ Mpc. The Galactic reddening toward the position of the SNe is $E(B - V) = 0.04$ mag (Schlegel et al. 1998).

2.5. SN 2011kf

SN 2011kf was first detected by CRTS (CSS111230:143658+163057) on 2011 December 30.5 UT (Drake et al. 2012). The spectra taken by Prieto et al. (2012) on 2012 January 2.5 UT and 17.5 UT reveal a blue continuum with absorption feature typical of a luminous Type Ic SN.

The closest galaxy is $\sim 23''$ S/W of the object position and is hence too far to be the host. There is no obvious host coincident with the position of this SN in SDSS DR9. We detect a faint host galaxy in deep *gri*-band images taken with the William Herschel Telescope on 2012 July 20. At a magnitude $r = 23.94 \pm 0.20$, this is too faint to affect the measurements of the SN flux out to +120 days. The redshift of the object has been determined to be $z = 0.245$ from narrow H α and [O III], equivalent to a luminosity distance of $d_L = 1204$ Mpc. The foreground reddening is $E(B - V) = 0.02$ mag from Schlegel et al. (1998).

2.6. SN 2012il

SN 2012il was first detected in the PS1 FGSS on 2012 January 19.9 UT (Smartt et al. 2012) and also independently discovered by CRTS on 2012 January 21 (CSS120121:094613+195028; Drake et al. 2012). On January 29 UT we obtained a spectrum of the SN, which resembled SN 2010gx four days after maximum light. The merged PS1 and CRTS data suggest a rise time of more than two weeks, different from that of SN 2010gx (Pastorello et al. 2010) but similar to PS1-11ky (Chomiuk et al. 2011). An initial analysis of observations from *Swift* revealed a marginal detection in the u , b , v , and $uvm2$ filters, with no detection in the $uvw1$ and $uvw2$ filters, or in X-rays (Margutti et al. 2012). However, our re-analysis of the *Swift* data reveals a detection above the 3σ level in the $uvw1$ and $uvw2$ filters (see Table A7). No radio continuum emission from the SN was detected by the EVLA (Chomiuk et al. 2012).

In our astrometrically calibrated images the SN coordinates are $\alpha = 09^h 46^m 12^s.91 \pm 0^s.05$, $\delta = +19^\circ 50' 28''.70 \pm 0''.05$ (J2000). This is within $0''.12$ of the faint galaxy SDSS J094612.91+195028.6 ($g = 22.13 \pm 0.08$, $r = 21.46 \pm 0.07$). The emission lines of H α , H β and [O III] from the host give a redshift of $z = 0.175$, corresponding to a luminosity distance of $d_L = 825$ Mpc. The Galactic reddening toward SN 2012il given by Schlegel et al. (1998) is $E(B - V) = 0.02$ mag, three times lower than the value reported by Margutti et al. (2012).

3. FOLLOW-UP IMAGING AND PHOTOMETRY

Optical and near-infrared (NIR) photometric monitoring of the five SNe was carried out using the telescopes and instruments listed in Appendix A. The main sources of our photometric follow-up were the SDSS-like *griz* filters in the cameras at the Liverpool Telescope (RATCam), the William Herschel Telescope (ACAM), and the Faulkes North Telescope (MEROPE). Further data in *BV* and *JHK* filters were taken for some of the SNe with the EKAR 1.8 m Telescope (AFOSC), the ESO NTT (EFOSC2) and the Nordic Optical Telescope (NOTCam). *Swift*+UVOT observations have been taken for four out of five SNe in the UV filters $uvw2$, $uvm2$, and $uvw1$ (and for three SNe in the *Swift* u filter) and we analyzed these publicly available data independently. Aside from SN 2011ke, ground-based SDSS-like u observations were sparse, and for two SNe of our sample nonexistent.

Observations were reduced using standard procedures in the IRAF¹⁶ environment. The magnitudes of the SNe, obtained through a point-spread function fitting, were measured on the final images after overscan correction, bias subtraction, flat field correction, and trimming. When necessary we applied a template subtraction technique (see Figure 1) on later epochs (through the HOTPANTS¹⁷ package based on the algorithm presented in Alard 2000). The instruments used to obtain reference images were the William Herschel Telescope and the Telescopio Nazionale Galileo. The same images were used to measure the host magnitudes and listed in Appendix A (Tables A1–A3, A5, and A6) and labeled as “Host.” When we did not have template images, we used SDSS images as templates to remove the flux of the host. The magnitudes of SDSS stars in the fields of

¹⁶ Image Reduction and Analysis Facility (IRAF) is distributed by the National Optical Astronomy Observatory, which is operated by the Association of Universities for Research in Astronomy, Inc., under cooperative agreement with the National Science Foundation.

¹⁷ <http://www.astro.washington.edu/users/becker/hotpants.html>

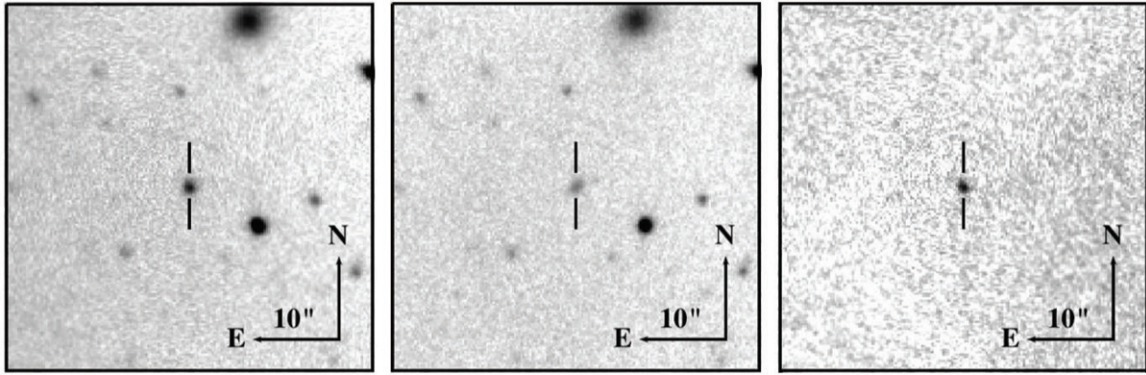


Figure 1. From left to right: PTF10hgi+host galaxy on MJD 55615.2, host galaxy on MJD 56075.0 used as template image and the final subtracted image showing the SN.

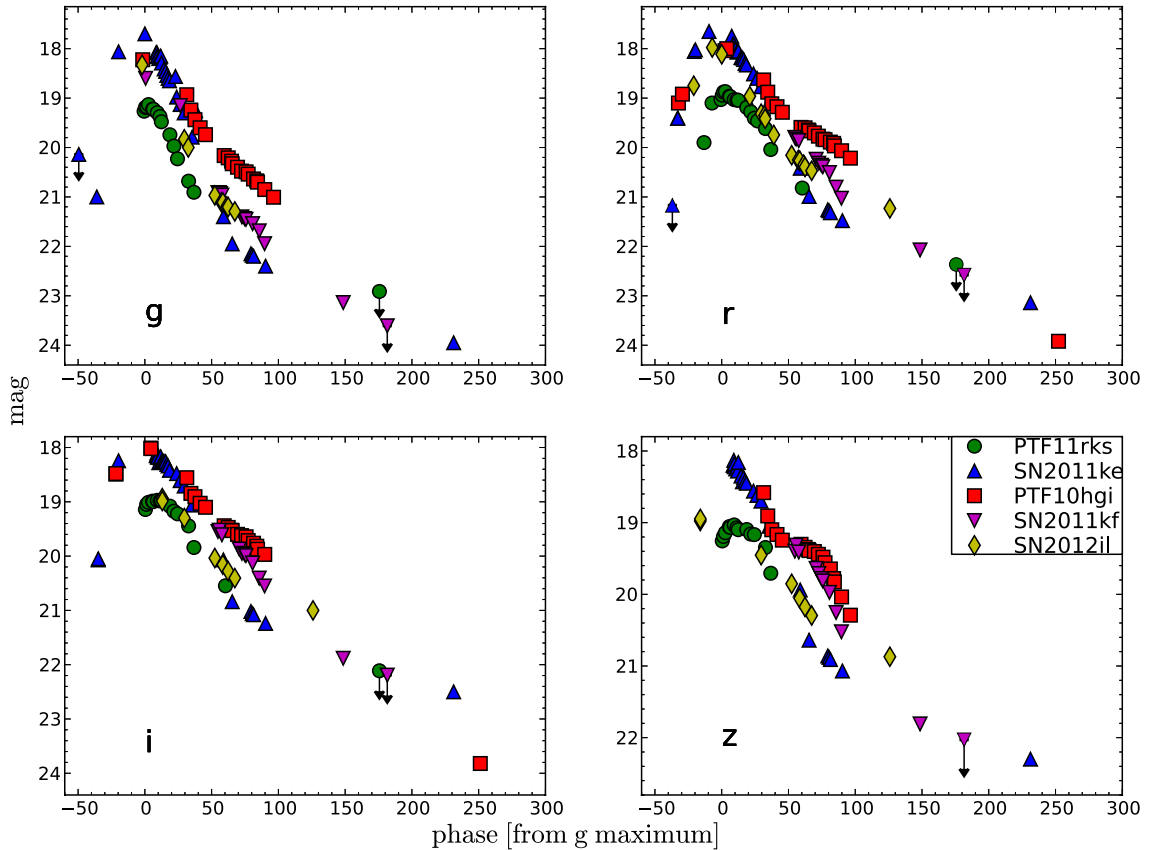


Figure 2. Observed *griz* light curves of PTF11rks (green circles), SN 2011ke (blue triangles), PTF10hgi (red squares), SN 2011kf (purple upside down triangles), and SN 2012il (gold diamonds). *V* magnitudes of SN 2011ke have been transformed in *r* through color transformation to better show the behavior around peak. The phase is from the respective maximum in the *g* band. Detections from the ATels are shown here and reported in Appendix A in Tables A1–A3, A5, and A6.

(A color version of this figure is available in the online journal.)

the transients were used to calibrate the observed light curves (Figure 2). All Sloan magnitudes—as well as the NTT *U* and *R* magnitudes—were converted to the SDSS AB magnitude system and color corrections were applied. PS1 magnitudes were also converted to SDSS magnitudes following the prescription in Tonry et al. (2012b). *B* and *V* magnitudes are reported in the Vega system. The PTF10hgi field was not covered by SDSS, so the average magnitudes of local sequence stars were determined on photometric nights, and subsequently used to calibrate the zero points for the non-photometric nights. Magnitudes of the local sequence stars are reported in Appendix B (Table A8) along with their rms (in parentheses).

For the *Swift* *u*-band data, we determined magnitudes in the UVOT instrumental system (Poole et al. 2008) and subsequently converted to Sloan *u* by applying a shift of $\Delta u \approx 0.2$ mag. The shift has been computed for each SN from a comparison of the magnitudes of the reference stars in the SNe fields in the UVOT and Sloan photometric systems. The only exception is PTF10hgi, where, due to the absence of ground-based *u* images, we applied the average shift of the other SNe. The UV magnitudes are reported in Appendix A (Table A7).

NIR observations are not shown in Figure 2 as these were only obtained for PTF11rks (see Table A4). The *JHK* photometry was calibrated to the Two Micron All Sky Survey system

(Vega-based), using the same local sequence stars as for the optical calibration. Thus, the values reported are Vega magnitudes.

3.1. Light Curves

3.1.1. PTF10hgi

Pre-peak observations are available only in the r band, suggesting a rise time comparable to SN 2011ke. PTF10hgi shows a bell-like-shaped light curve around peak. The post-maximum light curve shows a constant decline in all the bands until 40 days. After 40 days, the decline rate of PTF10hgi changes to have a slope similar to the decays shown by the other SNe. The change in the i -band slope is not as evident, while the z -band light curve is also dissimilar to the other bands. The magnitudes beyond 90 days are evaluated using the template subtraction with 646–648 day epochs as template images.

3.1.2. SN 2011ke

SN 2011ke was detected during the rise phase, and we continued to observe the SN until it disappeared behind the Sun in late 2011 August. The non-detection of the transient the day before the discovery gives us the best constraint on the explosion epoch of any SL-SN to date, allowing the rise time and light curve shape to be confidently measured. The light curve is bell-shaped around peak in the observed-frame g band, and more similar to the light curve of SCP-06F6 (Barbary et al. 2009). The post-maximum light decrease is slower at redder wavelengths, as in the previous object. It follows a constant slope until 50 days, when the slope changes to a slower decline. SN 2011ke then continued to fade at the same rate until the last available photometric point at ~ 200 days post-maximum. The reference template (339 days) was used to retrieve the magnitudes after 51 days.

3.1.3. PTF11rks

The transient was discovered just before the g -band peak. The pre-discovery limit of December 11 (Quimby et al. 2011a) indicates a rise time on the order of 20 days, followed by a slower decline post-maximum. The r -band light curve shows an asymmetric peak as for SNe 2005ap and 2010gx (Quimby et al. 2007; Pastorello et al. 2010), in contrast to the rounded peaks of the light curves of PS1-10awh and PS1-10ky (Chomiuk et al. 2011). The SN fades by ~ 2.1 mag over the first 30 days in the rest-frame g band, with a slower decline in the redder bands. The decrease is faster than that of the other SL-SNe Ic, although a more rapid decline at redder wavelengths is common in SNe (see Figure 1 in Pastorello et al. 2010). After 50 days the SN faded below our detection limit, even in deep imaging. A small, but non-negligible, flux contribution from the host has been found after 28 days and was removed using template subtraction with the reference images at 218 days. While for the i and z bands we used the SDSS images as template.

3.1.4. SN 2011kf

The light curve of SN 2011kf is the least well sampled as our monitoring started some 20 days after the ATel discovery announcement. We assume that the reported point of Drake et al. (2012) is at peak which is supported by the spectral and color evolution of the SL-SN during its subsequent evolution. During the first 50 days, the decline in the g band resembles those of the other SL-SNe Ic. But between 50 and 150 days, the decline rate changes markedly and the fading is slower. The reference

template (164 days) was used to retrieve the magnitudes after 71 days. Because of the proximity of the template epoch and last SN epoch, we also used SDSS images as a secondary template. The values retrieved with the two different templates were in agreement, strengthening simultaneously the lack of the SN at 145 days and the detection of the faint host in the deep images of 164 days.

3.1.5. SN 2012il

SN 2012il was discovered before it peaked in the g and r bands. The first two epochs available are in the PS1 z_{PI} band and the CSS unfiltered system (Drake et al. 2012). We cannot set a robust constraint on the rise time for SN 2012il, but it is likely at least two weeks. The shape of the light curve around peak in r band is possibly asymmetric as in PTF11rks and SN 2010gx, although we are somewhat constrained in this statement due to the uncertainty of the peak epoch. As for SN 2011ke, we see a clear change in the decline rate after 50 days, when SN 2012il has a slower decline (shown in Figure 2). This change in decline to a slower fading rate is illustrated with the latest detection in all three filters riz at ~ 113 days after peak. The reference template (327 days) was used to retrieve the magnitudes at 113 days and the g magnitudes after 58 days.

3.2. Absolute Magnitudes

In calculating absolute magnitudes (and subsequently bolometric magnitudes), we have assumed negligible internal host galaxy reddening for all the objects, and applied only foreground reddening, with the values reported in Section 2. No Na I D absorption features due to gas in the hosts were observed. However, we cannot exclude possible dust extinction from the hosts, therefore the absolute magnitudes reported here are technically lower limits. Given that the hosts are all dwarf galaxies, and the transients have quite blue spectra around peak, it appears that any correction would be small. We computed k -corrections for each SN using the spectral sequence we have gathered. For photometric epochs for which no spectra were available, we determined a spectral energy distribution (SED) using the multi-color photometric measurements available. This SED was then used as a spectrum template to compute the K -corrections. Comparisons between the two methods (K -correction directly from spectra, or with the photometric colors) showed no significant differences. We also determined K -corrections for SN2010gx using the spectral method and using photometric colors. Again we found consistency between the two methods. After applying foreground reddening corrections and K -corrections we estimated absolute rest-frame peak magnitudes (cf. Table 1).

In Figure 3, we compare the rest-frame g -band absolute light curves (in the AB system) of the SNe studied here with those of other low- z super-luminous events and the well-studied Type Ic SN 1998bw (Galama et al. 1998; McKenzie & Schaefer 1999; Sollerman et al. 2000; Patat et al. 2001). The epochs of the maxima were computed with low-order polynomial fits and by comparison of the light curves and their color evolution with those of other SL-SNe, and are listed in Table 1. The absolute peak magnitudes of PTF11rks and PTF10hgi are fainter than the bulk of SL-SNe, although they are still ~ 2 mag brighter than SN 1998bw. Interestingly, the two faintest SL-SNe Ic display different decline rates to each other, PTF11rks is similar to SN 2010gx whereas PTF10hgi decreases at a slower rate. The other three objects have peak magnitudes comparable with that of SN 2010gx ($M_g \approx -21.67$) and show a similar decline. The decline slope changes in 4 of the 5 objects after 50 days in

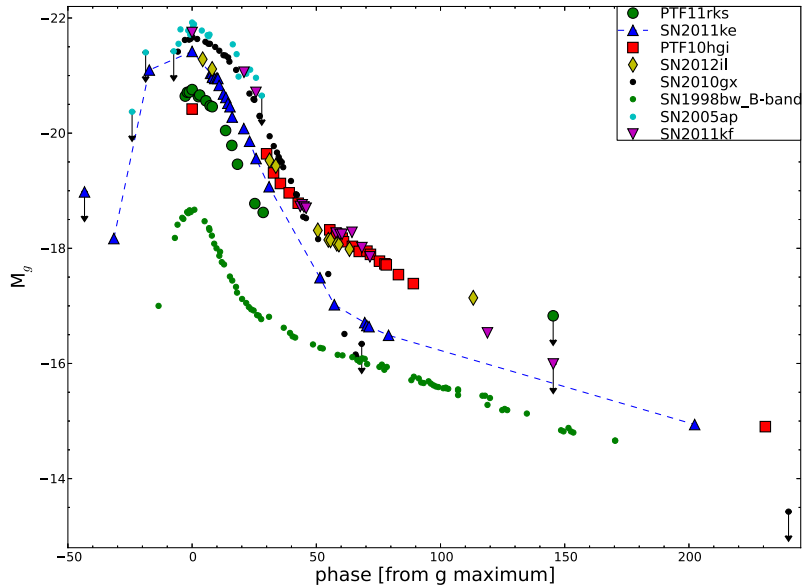


Figure 3. g -band absolute light curves of PTF11rks, SN 2011ke, PTF10hgi, SN 2011kf, and SN 2012il and a number of super-luminous events as well as the stripped envelope SN 1998bw. The light curves for each SN have been derived by correcting the observed broadband photometry for time dilation, distance modulus, foreground extinction, and differences in effective rest-frame bandpass (K -correction). The last PTF10hgi and SN 2012il points were converted from the r mag applying a color correction derived from SN 2011ke and SN 2011kf at similar epochs.

(A color version of this figure is available in the online journal.)

Table 1
Main Properties of the SN Sample

	PTF10hgi	SN 2011ke	PTF11rks	SN 2011kf	SN 2012il
Alternative names	PSO J249.4461+06.20815	PS1-11xk, PTF11idj, CSS110406: 135058+261642		CSS111230: 143658+163057	PS1-12fo CSS120121: 094613+195028
α (J2000.0)	16 ^h 37 ^m 47 ^s .08	13 ^h 50 ^m 57 ^s .78	01 ^h 39 ^m 45 ^s .49	14 ^h 36 ^m 57 ^s .64	09 ^h 46 ^m 12 ^s .91
δ (J2000.0)	06 [°] 12'29".35	26 [°] 16'42".40	29 [°] 55'26".87	16 [°] 30'57".17	19 [°] 50'28".70
z	0.100	0.143	0.190	0.245	0.175
Peak g (mag)	-20.42	-21.42	-20.76	-21.73	-21.56
$E(B - V)$ (mag)	0.09	0.01	0.04	0.02	0.02
L_{griz} peak ($\times 10^{43}$ erg s^{-1})	2.09	4.47	3.24	6.45	$\gtrsim 4.47$
Light curve peak (MJD)	55326.4 \pm 4.0	55686.5 \pm 2.0	55932.7 \pm 2.0	55925.5 \pm 3.0	55941.4 \pm 3.0
Host r (mag)	-16.50	-18.42	-19.02	-16.52	-18.18

the rest frame (while for the other, SN 2011ke, our data do not constrain it). The light curves then settle on a tail resembling the decay of ^{56}Co . This is apparent in Figure 3 as the tails of the SL-SNe are similar to that of SN 1998bw which is known to be powered by ^{56}Ni . The light curves follow the ^{56}Co decay within errors of 10%, the biggest discrepancy is for SN 2011kf which falls more rapidly between 100–200 days. SN 2007bi (Gal-Yam et al. 2009; Young et al. 2010) also followed the ^{56}Co decay at late times, but with a tail that is ~ 2 mag brighter than the SL-SNe Ic, and with a much slower overall evolution. We also note that the light curves of our objects flatten at slightly different epochs, with the tail for SN 2011ke commencing ~ 10 days after the last point in the light curve for SN 2010gx.

3.3. Color Evolution

We computed rest-frame color curves, after accounting for the reddening and redshift effects of time dilation and K -correction. The color curves are useful probes of the temperature evolution of the SNe. We also calculated rest-frame color evolution of SN 2010gx, the only other SL-SN Ic with a good coverage in SDSS filters at a similar redshift. In Figure 4, the SL-SNe show a constant color close to $g - r = 0$ from the pre-peak phase

to ~ 15 days. This evolution is similar to the color evolution of the higher redshift PS1-10ky in the observed bands $i_{P1}-z_{P1}$ (Chomiuk et al. 2011).

The constant color until 15 days implies that the SED does not evolve over these epochs. Up to maximum light, the spectra of these SL-SNe appear to be blue, with the only strong features being the O II lines in this range covered by the gr filters (Pastorello et al. 2010; Quimby et al. 2011b; Chomiuk et al. 2011; Leloudas et al. 2012). Hence this could be due to an approximately constant temperature. This is also illustrated in Figure 8 of Chomiuk et al. (2011) for the higher redshift PS1-10ky. Close to peak the O II lines disappear, leaving the spectra featureless for ~ 10 days, while after peak the temperature begins to decrease (see Section 5.1). A monotonic temperature decline between 14,000 K and 12,000 K (blackbody peak $2100 \text{ \AA} \lesssim \lambda \lesssim 2500 \text{ \AA}$) in objects with featureless spectra does not strongly affect the color evolution for $\lambda \gtrsim \lambda_{\text{peak}}$, as the slopes of blackbodies at these two temperatures are quite similar. To detect differences in temperature between a 12,000 K and a 14,000 K blackbody requires color curves which sample rest wavelengths below 3800 \AA , such as the $g - z$ color of PS1-10ky. Indeed this object did show an increase in $g - z$.

Table 2
Journal of Spectroscopic Observations

Date	MJD	Phase ^a (days)	Range (Å)	Resolution ^b (Å)	Instrumental Configuration
PTF11rks					
2012 Jan 9	55936.36	3.1	3400–9200	13	NOT+ALFOSC+Gm14
2012 Jan 17	55944.34	9.8	3500–9200	13	NOT+ALFOSC+Gm14
2012 Jan 26	55952.57	16.7	3500–9200	13	NOT+ALFOSC+Gm14
2012 Mar 3	55989.38	47.6	4300–8300	5	WHT+ISIS+R158R
SN 2011ke					
2011 May 15	55696.52	8.8	3300–10000	14	TNG+DOLORES+LRB,LRR
2011 May 22	55704.46	15.7	3400–9200	14	CAHA+CAFOS+b200
2011 Jun 1	55714.48	24.5	3300–10000	14	TNG+DOLORES+LRB,LRR
2011 Jun 9	55722.45	31.4	5100–9700	5	WHT+ISIS+R158R
2011 Jun 18	55731.49	39.4	3300–10000	14	TNG+DOLORES+LRB,LRR
2011 Jun 25	55738.49	45.5	3600–8800	16	NTT+EFOSC2+Gm13
SN 2012il					
2012 Jan 30	55956.53	12.8	3400–9200	13	NOT+ALFOSC+Gm14
2012 Mar 3	55989.51	40.9	5000–7800	5	WHT+ISIS+R300B,R158R
2012 Mar 17	56003.56	52.9	3000–23000	2	VLT+XSHOOTER
PTF10hgi					
2010 Jul 20	55398.41	32.7	3400–9200	14	CAHA+CAFOS+b200
2010 Aug 28	55436.53	67.4	3200–8000	16	GEMINI+GMOS+R150
2010 Sep 11	55451.37	80.9	3200–8300	10	WHT+ISIS+R300B,R158R
SN 2011kf					
2012 Jan 30	55956.74	25.1	3400–9200	13	NOT+ALFOSC+Gm14
2012 Mar 3	55989.75	51.6	4700–8300	10	WHT+ISIS+R158R

Notes. The telescope abbreviations are the same as used in Appendix A in Tables A1–A3, A5, and A6 plus TNG = 3.6 m Telescopio Nazionale Galileo + DOLORES; CAHA = 2.2 m Telescope at Calar Alto Observatory + CAFOS; VLT = 8.2 m ESO Very Large Telescope + XSHOOTER; GEMINI = 8.2 m Gemini Telescope North + GMOS.

^a Phases with respect to the g -band maxima and corrected for time dilation.

^b FWHM of night sky emission lines.

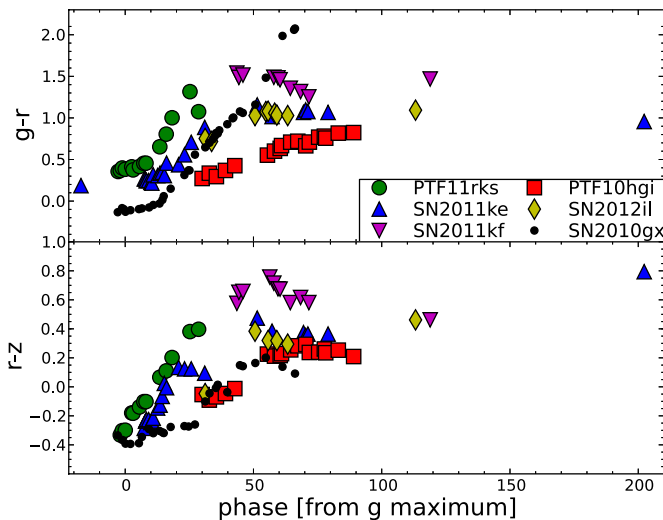


Figure 4. Comparison of the dereddened and K -corrected color evolution. PTF11rks, SN 2011ke, SN 2012il, PTF10hgi, and SN 2011kf are shown together with the well-sampled SN 2010gx.

(A color version of this figure is available in the online journal.)

After this early period of constant color, the $g-r$ color increases, reaching another phase of almost constant value at ~ 40 days, perhaps indicating a decrease in the cooling rate. There are some exceptions to this behavior, as seen for PTF11rks

and PTF10hgi. The $g-r$ color of PTF11rks increases earlier and with a steeper slope than the other SNe, but unfortunately our data stop before the possible second period of constant color. In contrast, the $g-r$ color for PTF10hgi increases much more slowly, and only reaches the possible late constant phase at ~ 80 days.

The $r-z$ colors of the sample show a roughly constant increase from peak to ~ 50 – 60 days, when the color evolution appears to flatten. The two exceptions are again PTF11rks and PTF10hgi; the former increases in $r-z$ more rapidly than the other objects, whereas the latter does not become as red, and experiences a clear decrease in $r-z$ after 80 days. The $r-z$ color evolution of SN 2010gx is similar to that of SN 2011ke and PTF10hgi.

3.4. Temperature Evolution

In Figure 5 the evolution of the temperature is plotted. This is derived from a blackbody fit to the continuum of our spectra (see Section 5), and compared to those of SN 2010gx and SN 2007gr. We also fit color temperatures at rest frame with a blackbody and the measurements are in good agreement with those from spectra.

Only PTF11rks has a good temperature coverage around peak, whereas our spectroscopic data are not well sampled at that phase. While we cannot clearly confirm the apparent constant temperature seen in SN 2010gx until ~ 10 days, the epochs at either side of ± 10 days are suggestive of a roughly

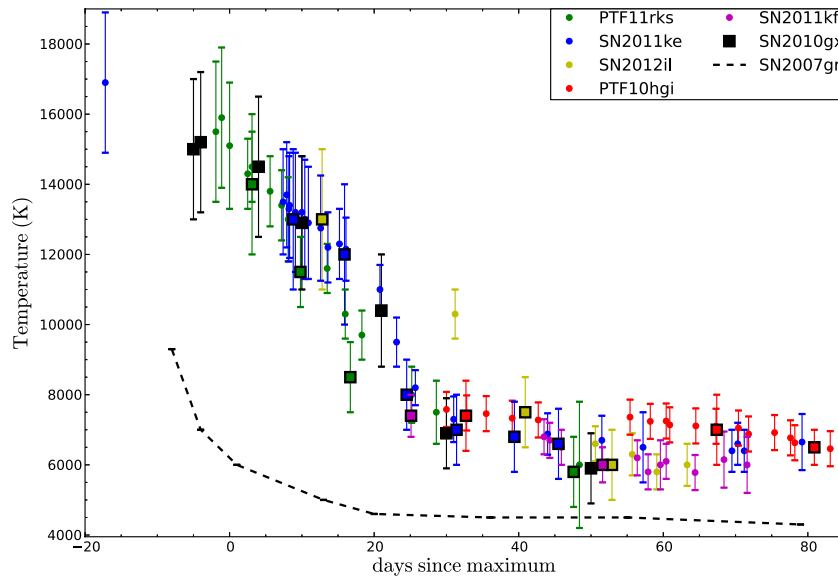


Figure 5. Evolution of the continuum temperature of PTF11rks (green), SN 2011ke (blue), SN 2012il (gold), PTF10hgi (red), and SN 2011kf (purple) are reported with those of SN 2010gx (black). The dashed black line shows the temperature evolution in the normal Type Ic SN 2007gr. The dots denote measurements from photometry, whereas squares are spectroscopic measurements.

(A color version of this figure is available in the online journal.)

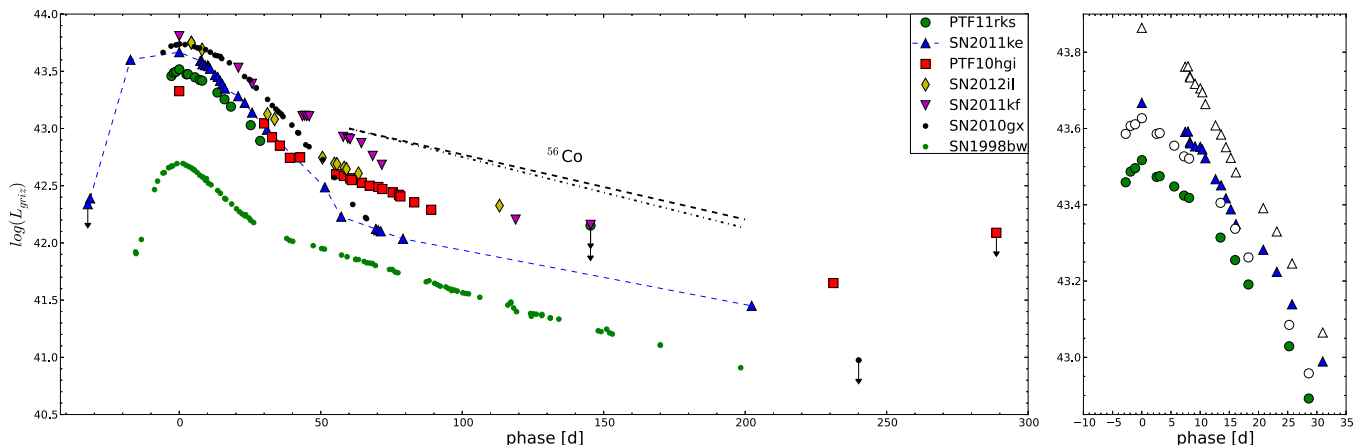


Figure 6. Left: *griz* bolometric light curves of PTF11rks, SN 2011ke, PTF10hgi, SN 2011kf, SN 2012il, SN2010gx, and the Type Ic SN 1998bw (*BVRi* bolometric light curve). These bolometric light curves are computed after correcting the observed broadband photometry for time dilation and applying *K*-corrections. The dashed line is the slope of ^{56}Co to ^{56}Fe decay and the dot-dashed line is the decay slope with a 10% error. Right: comparison between the *griz* bolometric light curve (filled symbols) and the *UVgriz* bolometric light curve of PTF11rks and SN 2011ke which include the measured UV flux from *Swift* photometry.

(A color version of this figure is available in the online journal.)

constant temperature phase. After ~ 10 days a clear decline in temperature is seen, with a rate of decline of ~ 2500 K over 10 days. This decline continues until the SN reaches a constant temperature of ~ 6000 K prior to, and during, the pseudo-nebular phase.

4. BOLOMETRIC LUMINOSITY

Simultaneous UV–optical–NIR photometry at all epochs is required to obtain a direct measurement of the bolometric luminosity. This is typically difficult to attain at all epochs during an SN light curve, and we do not have complete wavelength coverage for the five SL-SNe. Nevertheless, valid corrections can be applied to the observed photometric bands to compute the bolometric flux.

The effective temperatures of the photospheres of SL-SNe Ic during their first 30–50 days after explosion are between

$T_{\text{bb}} \sim 13,000$ and $19,000$ K (see Table A6 and Pastorello et al. 2010; Chomiuk et al. 2012). This means that their fluxes are significant in the UV ($\lambda < 3000$ Å) during this period while our *griz* bands typically cover from rest-frame 3800 Å redward. Thus a significant fraction of the flux is not covered by the optical *griz* imaging. At around 20 days after peak, the effective temperatures tend to drop below $10,000$ K, hence the SEDs peak between 3000 Å and 4000 Å. Although the peak of the SED moves redward, a significant amount of the bolometric flux is radiated in the UV even during these late stages. In the following, we will use the term “*griz*-bolometric light curve” to refer to a bolometric light curve determined using only the specified filters (in this example, *griz*) with the flux set to zero outside the observed bands.

Initially, the broadband magnitudes in *griz* were converted into fluxes at the effective filter wavelengths, then were corrected for the adopted extinctions (cf. Section 2). An SED was then

computed over the wavelengths covered and the flux under the SED was integrated assuming there was zero flux beyond the integration limits. Fluxes were then converted to luminosities using the distances previously adopted. We initially determined the points on the *griz*-bolometric light curves at epochs when *griz* were available simultaneously (or very close in time). For epochs with coverage in less than the four filters we were able to estimate the *griz*-bolometric light curves. Magnitudes from the missing bands were generally estimated by interpolating the light curves using low-order polynomials between the nearest points in time. For some points this interpolation was not possible and we used one of two methods. The first was an extrapolation assuming constant colors from neighboring epochs and the second was using colors from the other SL-SNe at similar epochs. For example, we used the latter method for the last point on the light curve for PTF10hgi. The *griz*-bolometric light curves estimated using this technique are plotted in the left panel of Figure 6.

Useful *Swift* photometry for UV flux measurements exists for PTF11rks and SN 2011ke (see Table A7), which allow us to compare the *griz*-bolometric light curves and the *UVgriz*-bolometric light curves (pseudo-bolometric hereafter), where the *UV* component is determined from the *uvw2*, *uvm2*, and *uvw1* filters covering 1800–3000 Å. The difference between these two bolometric light curves, with and without the radiated energy below 3500 Å, is shown in the right panel of Figure 6.

Inclusion of the *Swift* photometry results in maximum luminosities for PTF11rks and SN 2011ke of $L \approx 4.27 \times 10^{43}$ erg s⁻¹ and $L \approx 7.08 \times 10^{43}$ erg s⁻¹, respectively. Hence the *griz*-bolometric fluxes are a factor 1.5 lower than when including the 1800–3000 Å range covered by *uvw1*–*uvw2* filters. While one could fit a blackbody curve to the observed *griz* SEDs (or the spectra) and integrate under the curve to determine the emitted total flux across all wavelengths, this would not account for the strong line absorption shown in the rest-frame UV spectra (for example, clearly seen in the high-*z* objects of Chomiuk et al. 2011). Hence from here on we will use *griz*-bolometric light curves for consistency on all objects, but we should bear in mind the additional contribution from the rest-frame UV that we have quantified in the right-hand panel of Figure 6. The maximum luminosities reached by our computed *griz*-bolometric light curves are $L_{\text{PTF11rks}} \approx 3.24 \times 10^{43}$ erg s⁻¹, $L_{\text{SN2011ke}} \approx 4.47 \times 10^{43}$ erg s⁻¹, $L_{\text{SN2011kf}} \approx 6.45 \times 10^{43}$ erg s⁻¹, $L_{\text{SN2012il}} \gtrsim 4.47 \times 10^{43}$ erg s⁻¹, and $L_{\text{PTF10hgi}} \approx 2.09 \times 10^{43}$ erg s⁻¹. As expected, these are lower than those reported by Chomiuk et al. (2011) for the $z \simeq 0.9$ objects PS1-10ky and PS1-10awh due to the lack of rest-frame UV coverage for our low-redshift sample.

The comparison in Figure 6 further quantifies the large bolometric luminosities of these SL-SNe Ic—as discussed by Pastorello et al. (2010), Quimby et al. (2011b), Chomiuk et al. (2011), and Leloudas et al. (2012). There is clearly some diversity in the light curve peaks and widths. The low redshift of these objects makes it possible to follow the evolution beyond 100 days after peak for the first time. Only 1 other object (SN 2010gx) has been investigated in this phase (Pastorello et al. 2010; Chen et al. 2013) and no detection was found at greater than 100 days. Quantifying the host contribution and using image subtraction to recover the SL-SN flux in these late phases is essential (as discussed in Section 3). It transpires that SL-SNe Ic show a large diversity in this phase, quite different to the relatively homogenous behavior around peak. After 50 days post-maximum, all 4 of the SL-SNe Ic for which we have data

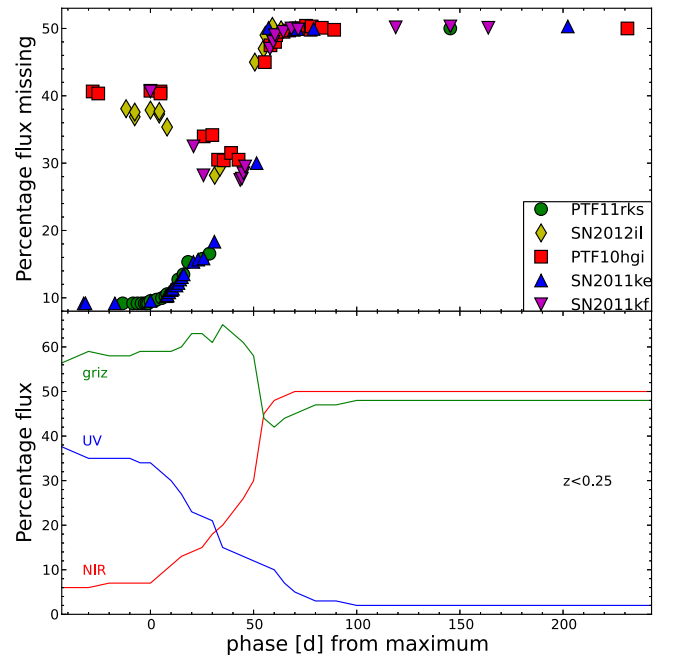


Figure 7. Top: percentage of flux missed, assuming a blackbody fit, in NIR by SN 2011ke and PTF11rks, and in UV+NIR by PTF10hgi, SN 2011kf, and SN 2012il (the regions not covered by our photometry for each object). Bottom: average percentage of the bolometric flux in UV (blue), optical (green), and NIR (red) for a representative SL-SN Ic at $z < 0.25$.

(A color version of this figure is available in the online journal.)

(SN 2011ke, SN 2012il, SN 2011kf, and PTF10hgi) show an abrupt change in the slope of the *griz*-bolometric light curve. The slope flattens and is quite similar to that of the decay of ⁵⁶Co to ⁵⁶Fe. SN 2011ke and PTF10hgi appear to decline even slower than the ⁵⁶Co slope.

Additionally, at these later phases we know from detailed coverage of CCSNe that a significant amount of radiation will be emitted in the NIR when the photospheric temperature drops below 10,000 K. This flux can mostly be captured by *JHK* photometric observations. As we lack this complete wavelength coverage for our SL-SNe, we employed an SED method to determine the correction. We use the photospheric temperatures (derived in Section 3.4) to derive simple blackbody SEDs and integrate the flux redward of the rest-frame *z* band. The flux missed in the NIR by our *griz*-bolometric measurements typically increases with time, and reaches roughly 50% after ~60 days post-maximum. We plot the rest-frame NIR contributions as an average of all the SL-SNe presented here, for a representative redshift of $z < 0.25$, in the bottom panel of Figure 7. The optical component refers to the *griz* bands (green line), and the NIR contribution beyond the *z* band is denoted with the red line. We also used this method to have a secondary estimate of the UV contribution (blue line). In this case we integrated the flux under the blackbody spectra below the *g* band. We compared the UV flux contribution with those evaluated from the two SNe which have *Swift* UV photometry and find that the two are consistent within the errors. Figure 7 summarizes the flux contributions from the different wavelength regimes and allows the *griz*-bolometric light curves to be corrected when required.

If these tail phase luminosities were powered by ⁵⁶Co then it would require that there is full γ -ray trapping in the ejecta. This is not typically seen in Type Ic SNe. For example, the *BVRI* bolometric light curve of SN 1998bw is shown for comparison which decays faster than the nominal ⁵⁶Co half-life. Sollerman

et al. (2000) showed that if one assumes a fixed energy source (i.e., some mass of ^{56}Co), then the trapping efficiency decreases with time ($\propto t^{-2}$). Hence at the epochs of these SL-SNe (100–200 days) only around $\sim 45\%$ of the γ -rays would be trapped if they had similar ejecta mass and density profiles to other Type Ic SNe. This seems to be in contradiction to the measured slopes which appear to either follow the ^{56}Co decay timescale or even be slightly shallower. Despite this issue, we shall initially assume (for illustrative purposes) that the tail phases are actually powered solely by radioactive decay. This allows a corresponding mass of ^{56}Ni to be determined. Later in this paper we shall show that the tail phase luminosity may be powered by magnetar energy injection rather than ^{56}Co decay. Although four of the SL-SNe do show a flattening in their luminosity, it appears SN 2010gx does not, at least not at the detectability level of Chen et al. (2013). The data we have for PTF11rks do not allow a conclusion.

We initially make the assumption that γ -rays from ^{56}Co decay are fully thermalized during the full durations of the light curves we measure. We know that for typical SN Ic ejecta this is not the case, but it allows us to derive illustrative masses for ^{56}Co powering. The ^{56}Ni masses can thus be estimated using the formula

$$M(^{56}\text{Ni})_{\text{SN}} = 7.87 \times 10^{-44} L_t e^{\left[\frac{(t-t_0)/(1+z)-6.10}{111.26}\right]} M_{\odot} \quad (1)$$

(e.g., as employed by Hamuy 2003), where t_0 is the explosion epoch, 6.1 days is the half-life of ^{56}Ni , and 111.26 days is the e -folding time of the ^{56}Co decay, which release 1.71 MeV and 3.57 MeV, respectively, as γ -rays (Woosley et al. 1989; Cappellaro et al. 1997).

This method gives ^{56}Ni masses of $M(^{56}\text{Ni})_{\text{SN2011ke}} \sim 0.5 M_{\odot}$, $M(^{56}\text{Ni})_{\text{SN2012il}} \sim 1.2 M_{\odot}$, $M(^{56}\text{Ni})_{\text{PTF10hgi}} \sim 1.1 M_{\odot}$, while for SN 2011kf we retrieved an approximate $M(^{56}\text{Ni})_{\text{SN2011kf}} \lesssim 1.9 M_{\odot}$. The measured decline for SN 2011kf was slightly steeper than the fully trapped ^{56}Ni tail. We also estimated an upper limit $M(^{56}\text{Ni})_{\text{PTF11rks}} \sim 1.3 M_{\odot}$ for PTF11rks based on the last epoch in which the SN was detected. These values should be considered as lower limits because of our limited rest-frame wavelength coverage. At this phase, the contribution from the NIR plays an important role in the bolometric luminosity of SNe, as described above. Indeed, the SED of SN 1987A (data from Hamuy et al. 1988; Bouchet et al. 1989) also suggests that as much as 50% of the total flux for our transients could be outside the *griz* bolometric light curves (at these epochs SN 1987A has already reached a constant temperature in the tail phase). Thus, to obtain a truer idea of the ^{56}Ni mass required to power these tail phases, the measured luminosities should be increased by roughly a factor two. In summary, we find that *if the luminosity in the tail phase is powered by ^{56}Co* then the ejected ^{56}Ni values required to power the light curves lie between $1.0 M_{\odot}$ and $2.4 M_{\odot}$, with an upper limit of $3.8 M_{\odot}$ for SN 2011kf. These ^{56}Ni masses cannot power the peak of the light curves, as shown by Pastorello et al. (2010), Quimby et al. (2011b), Chomiuk et al. (2011), and Leloudas et al. (2012). As we discuss below, we consider that the luminosity we detect in this phase is not necessarily due to radioactive ^{56}Co decay energy injection.

5. SPECTROSCOPY

All spectra were reduced (including trimming, overscan, bias correction, and flat-fielding) using standard routines within IRAF. Optimal extraction of the spectra was adopted to improve

the final signal-to-noise ratio (S/N). Wavelength calibration was performed using the spectra of comparison lamps acquired with the same configurations as the SN observations. Atmospheric extinction correction was based on tabulated extinction coefficients for each telescope site. Flux calibration was performed using spectrophotometric standard stars observed on the same nights with the same setup as the SNe. The flux calibration was checked by comparison with the photometry, integrating the spectral flux transmitted by standard *griz* filters and adjusted by a multiplicative factor when necessary. The resulting flux calibration is accurate to within 0.1 mag.

The collected spectra are shown in Figure 8 (see Table 2) together with the spectra of SN 2010gx (Pastorello et al. 2010) for comparison. A version with all the spectra convolved to the same resolution and binned to the same pixel scale is shown in Appendix C. In our spectroscopic sample we do not have pre-peak spectral coverage, which typically shows C II, Si III, and Mg II at UV wavelengths ($< 3000 \text{ \AA}$) and O II in the optical region (Quimby et al. 2011b). The only lines which we may expect to be visible in our wavelength regions (namely O II) have already disappeared by ~ 3 –12 days. At those epochs the SL-SNe spectra are featureless with the notable exception of PTF11rks, which shows weak broad absorption profiles of heavy elements such as Fe II, Mg II, and Si II between 3000 \AA and 6500 \AA . A weak Ca II H&K absorption line is barely detected in PTF11rks, as is the case for SN 2011ke and SN 2012il. Redward, Mg II $\lambda 4481$ and the Fe II multiplet $\lambda \lambda 4924, 5018, 5169$ are visible in PTF11rks. Other Fe II lines are barely visible in the region around 4500 \AA , while a shallow absorption due to Si II $\lambda 6347$ is also present. None of these lines are clearly detectable in SN 2011ke and SN 2012il at a similar phase.

Two weeks after maximum, SN 2011ke shows Mg II, Fe II, and Si II lines together with a clearer Ca II feature, albeit still shallower than for PTF11rks. The spectra obtained around 30 days for SN 2011kf and PTF10hgi have a low S/N of ~ 10 which makes line analysis problematic. However, the comparison with the other spectra indicates broad absorption profiles from Mg II and Fe II. The only line visible in the red part of the spectrum ($> 7000 \text{ \AA}$) is O I $\lambda 7775$ in SN 2011ke.

From ~ 30 days after maximum onward there is no strong evidence of new broad features emerging blueward of 8000 \AA , with the exception of the rise of Mg I $\lambda 4571$. The absorption lines of Mg and Fe become shallower, resulting in the emission components becoming more prominent from ~ 50 days onward. The Fe II emission line at $\sim 5200 \text{ \AA}$ is broader than Mg I λ suggesting it may be a blend.

The only exception to this general trend is PTF10hgi. In the last two available spectra PTF10hgi shows Ca II H&K (possibly blended with Mg II), three distinct absorptions related to the individual components of the Fe II multiplet ($\lambda \lambda 4924, 5018, 5169$) and Na I D $\lambda \lambda 5890, 5896$. Although the spectral evolution is relatively homogeneous, two of the samples have noticeable differences. In the first two weeks of evolution of PTF11rks the absorption line strengths look stronger, with $\overline{EW}_{\text{PTF11rks}} \sim 4 \times \overline{EW}_{\text{SL-SNe Ic}}$. The later phase line formation in PTF10hgi also looks different, with narrower absorption lines more similar to velocities seen in Type Ic SNe (see the comparison with SN 2007gr in Figure 10) Weak, narrow emission lines ($H\alpha$, $H\beta$, and [O III] $\lambda 4959, \lambda 5007$) from the host galaxies are also visible in all spectra, except those of PTF10hgi. These will allow metallicity and star formation rate measurements in the host, which is underway in a companion paper (T.-W. Chen et al., in preparation).

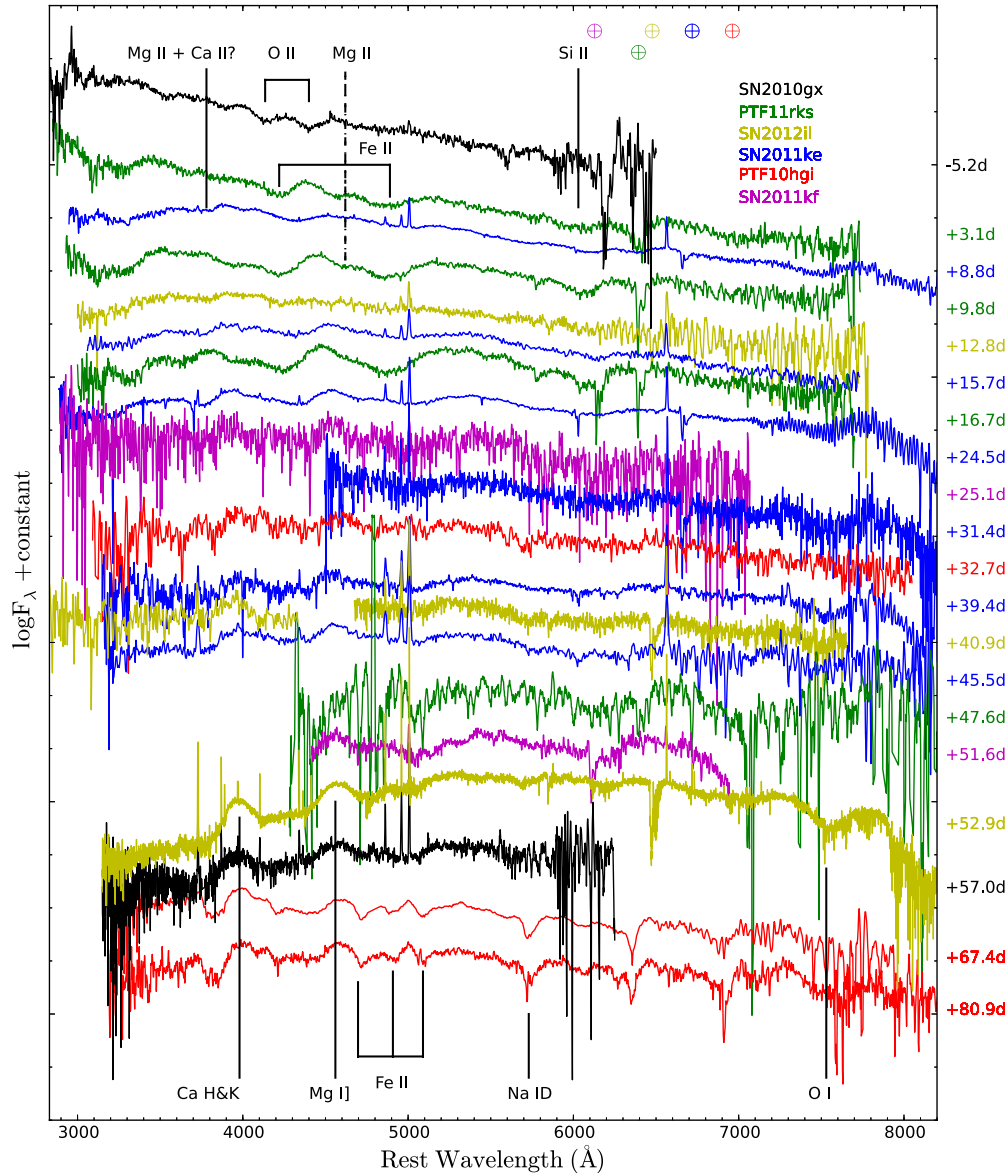


Figure 8. Spectra of PTF11rks are in green, SN 2011ke in blue, SN 2012il in gold, PTF10hgi in red, SN 2011kf in magenta, and SN 2010gx (Pastorello et al. 2010) in black. The phase of each spectrum relative to light curve peak in the rest frame is shown on the right. The spectra are corrected for Galactic extinction and reported in the rest frames. The \oplus symbols mark the positions of the strongest telluric absorptions. The most prominent features are labeled.

(A color version of this figure is available in the online journal.)

Figure 9 shows the complete spectrum of SN 2012il taken at ~ 53 days with VLT+XShooter, which has the widest wavelength coverage for SL-SNe obtained to date. As previously mentioned, blueward of 8000 \AA , Ca II H&K, Mg I], shallow Fe II and O I are present. A strong Ca II NIR triplet $\lambda\lambda 8498, 8542, 8662$ is visible, with the bulk of the absorption component at $v = 12000 \pm 2500 \text{ km s}^{-1}$. This is higher than the other absorption components (e.g., O I $v \sim 9500 \text{ km s}^{-1}$) and comparable with the velocities of the broad emission components of Ca II H&K, Mg I]. At about 7300 \AA a weak emission line is evolving and we tentatively identify it as [Ca II] $\lambda\lambda 7291, 7324$ emission feature. This line has not been detected before in an SL-SN Ic, probably due to the lack of high-quality spectra beyond 50 days after peak and the slow evolution of these SNe. The presence of [Ca II] and the emission lines around 4500 \AA imply that the SNe are evolving slowly toward the nebular phase. This seems to coincide with the change in slope of the light curve. In the NIR the $S/N \sim 5$ in the continuum is less than in the optical

($S/N \sim 30$), although it is still adequate to identify the strongest lines. We identify Mg II around 9200 \AA and Mg I $\lambda 15024$, although the last identification is less certain due to the low S/N and the proximity of a strong telluric feature. Most significantly, we identify He I $\lambda 10830$, the first sign of the presence of He in this group of SL-SNe Ic. We note that the only other ions which have transitions at this wavelength are Ar II, Fe I, Si I, and C I. These are expected to be intrinsically weaker than He I. There are no strong skylines at the observed position of this line $\sim 12725 \text{ \AA}$. Although we do not see other He I lines in the spectrum, this is not unexpected. In the Case B recombination in the temperature regime $T < 10,000 \text{ K}$ and electron density $10^2 \leq n_e \leq 10^6$ —the $\lambda 10830$ line is expected to be stronger than $\lambda 5876$ line (the strongest in the optical region) by a factor 2–10.

The spectral evolution of the SL-SNe sample in this paper provides additional information to that reported in Pastorello et al. (2010). In the top panel of Figure 10 the comparison

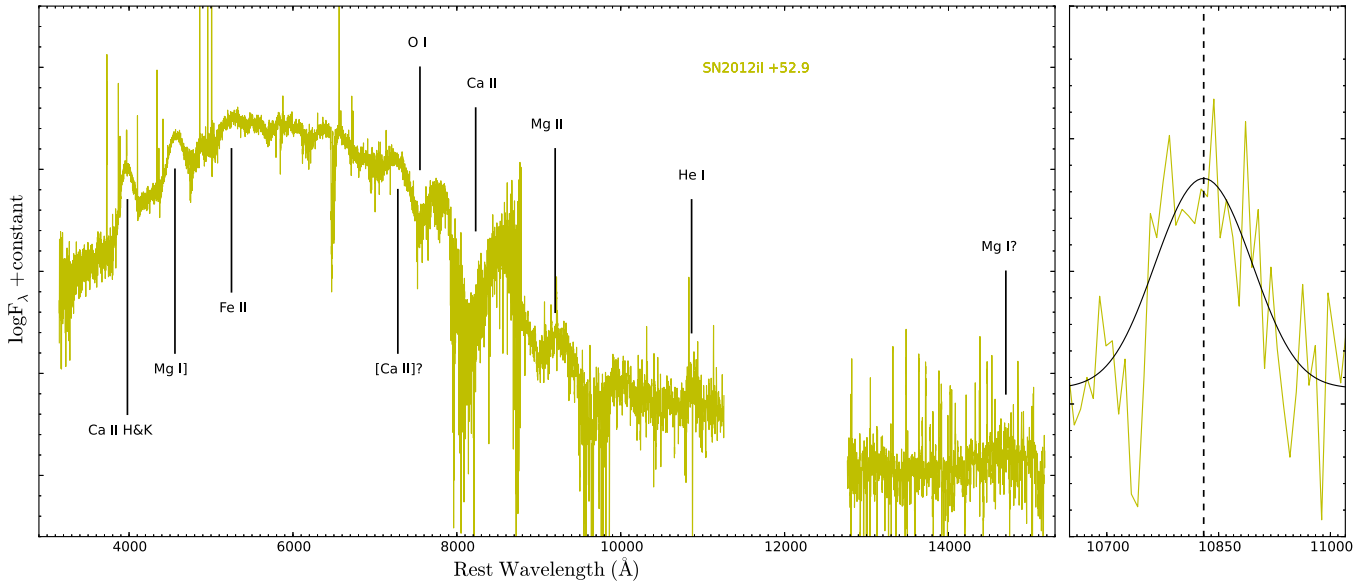


Figure 9. Spectrum of SN 2012il at ~ 53 days post-maximum. The spectrum is corrected for Galactic extinction and reported in its rest frame. The most prominent features are labeled. In the right panel a zoom of the He I line (spectrum binned by a factor 10) is shown with the Gaussian fit of the line. The dashed vertical line marks the expected position of He I $\lambda 10830$.

(A color version of this figure is available in the online journal.)

of the early-time spectra with those of SN 2010gx (Pastorello et al. 2010), and the Type Ic SNe 1994I (Baron et al. 1996) and 2004aw (Taubenberger et al. 2006) highlights a difference in the line evolution between PTF11rks and other SL-SNe. The spectrum at 9.8 days is similar to that of a Type Ic close to maximum light showing a faster transition to Type Ic SNe than the others. In contrast, other SL-SNe such as SN 2011ke match normal Type Ic SNe only after ~ 30 days (Figure 10, middle panel), resembling the spectral transition of SN 2010gx at this epoch. This makes the temporal evolution of PTF11rks very similar to those of canonical SNe Ic. Again the low S/N of the spectrum of PTF10hgi (32.7 days) precludes a precise analysis, although there are hints of a peculiar line evolution at wavelengths redder than 5500 \AA . In the bottom panel, SN 2010gx resembles SN 2004aw at ~ 10 days after peak whereas PTF10hgi matches normal Type Ic SNe at ~ 30 days, with a good match to SN 2007gr. From this comparison, it appears that PTF11rks and PTF10hgi evolve to into Type Ic SN on timescales of about 20 days quicker than other SL-SNe. The “fainter” luminosity ($M > -21$) of these two objects and their faster evolution to Type Ic SNe may provide another clue to understand the evolutionary path of these transients. It appears from these objects that the lower the peak luminosity, the faster the evolution of the photospheric spectra, with a time delay of 10 days to the Type Ic phase instead of the usual 30 days shown by most SL-SNe Ic.

5.1. Expansion Velocity

The expansion velocities measured for PTF11rks, SN 2011ke, SN 2012il, PTF10hgi, and SN 2011kf are reported in Table 3, and are compared with those of SN 2010gx and the standard Type Ic SN 2007gr (Hunter et al. 2009) in Figure 11. In the photospheric phase these were derived from the minima of the P Cygni profiles and their errors were established from the scatter between several independent measurements. During the phase in which the objects appear to be transitioning to the nebular phase (i.e., beyond about 50 days) the velocities were computed

as the FWHM of the emission lines (we will call this the pseudo-nebular phase). These are not tracers of the photospheric velocity and are reported for completeness; they will be discussed further in Section 6.2. We used Fe II $\lambda 5169$, Mg II $\lambda 4481$, and O I $\lambda 7775$ to measure velocities during the photospheric phase, and Ca II H&K and Mg I $\lambda 4571$ during the pseudo-nebular phase. The Fe II velocity evolution monotonically declines for all transients, ranging from $\sim 18,000 \text{ km s}^{-1}$ around peak to $\sim 8000 \text{ km s}^{-1}$ at 50 days. After this epoch we have only PTF10hgi spectra, and they still show clear absorption components of Fe II. The decline in velocity is faster and it reaches $\sim 4600 \text{ km s}^{-1}$ at the last epoch of 80 days, which is quite similar to the Fe II velocity of SN 2007gr. Mg II in the photospheric phase is always seen at higher velocity than Fe II, and decreases linearly by $\sim 1000 \text{ km s}^{-1}$ every 10 days. The O I velocity is comparable with that of Fe II, with the exception of SN 2011ke where it is slower than all other ions (albeit with large uncertainties due to the low S/N). Ca II and Mg I appear after ~ 40 days from maximum light and show the same intensity and velocity of $\sim 11,000 \text{ km s}^{-1}$ in the entire sample.

The PTF10hgi spectra after 60 days show Ca II absorption at late epochs, similar to normal Type Ic SNe. Figure 11 shows evidence for decreasing line velocity with time, especially from 10 days post-peak as seen for SN 2010gx (previously reported as a comparison in Chomiuk et al. 2011). Our analysis shows a clear sign of change in the rate of photospheric expansion (30–40 days), with a decline which resembles that typically observed during the photospheric phase of a CCSN explosion.

6. ON THE NATURE OF SL-SNe Ic

The SN sample presented in this paper provides new data for understanding the nature of super-luminous events. The similarity within this family is well established: high luminosity, similar spectral evolution, and an origin in faint host galaxies. The overall spectral evolution is indeed similar to that of SNe Ib/c, although SL-SNe spectroscopically evolve on a much longer timescale. However, the observed parameters of SL-SNe

Table 3

Observed Blackbody Temperature, Expansion Photospheric Velocities from Fe II $\lambda 5169$, Mg II $\lambda 4481$, and O I $\lambda 7775$ in our SL-SNe Sample on the Left; Expansion Velocities from Ca II H&K and Mg I] $\lambda 4571$ on the Right

Date	MJD	Phase ^a (days)	T (K)	v (Fe II) (km s ⁻¹)	v (Mg II) (km s ⁻¹)	v (O I) (km s ⁻¹)	v (Ca II) (km s ⁻¹)	v (Mg I]) (km s ⁻¹)
PTF11rks								
2012 Jan 9	55936.36	3.1	14000 ± 2000	17800 ± 2000	19000 ± 3000			
2012 Jan 17	55944.34	9.8	11500 ± 1000	17200 ± 2000	18000 ± 2000			
2012 Jan 26	55952.57	16.7	8500 ± 1000	16800 ± 2000	17000 ± 2000			
2012 Mar 3	55989.38	47.6	5800 ± 1000					
SN 2011ke								
2011 May 15	55696.52	8.8	13000 ± 2000	17800 ± 3000	19000 ± 3000	12000 ± 2000		
2011 May 22	55704.46	15.7	12000 ± 2000	13500 ± 2000	17000 ± 3000			
2011 Jun 1	55714.48	24.5	8000 ± 1000	12500 ± 1000	16000 ± 2000	9500 ± 2000		
2011 Jun 9	55722.45	31.4	7000 ± 1000					
2011 Jun 18	55731.49	39.4	6800 ± 1000	12000 ± 1000		9000 ± 2000		10000 ± 1500
2011 Jun 25	55738.49	45.5	6600 ± 1000	9800 ± 1500		8500 ± 2000	10000 ± 1500	10000 ± 1500
SN 2012il								
2012 Jan 30	55956.53	12.8	13000 ± 2000	17500 ± 2000				
2012 Mar 3	55989.51	40.9	7500 ± 1000	10000 ± 2000				
2012 Mar 17	56003.56	52.9	6000 ± 1000			9500 ± 1500	12000 ± 2500	12000 ± 2500
PTF10hgi								
2010 Jul 20	55398.41	32.7	7400 ± 1000					
2010 Aug 28	55436.53	67.4	7000 ± 1000	5200 ± 300			8300 ± 800	9800 ± 1000
2010 Sep 11	55451.37	80.9	6500 ± 500	4600 ± 300		7900 ± 1000	8000 ± 800	9500 ± 1000
SN 2011kf								
2012 Jan 30	55956.74	25.1	7400 ± 1000	12000 ± 3000				
2012 Mar 3	55989.75	51.6	6000 ± 1000	8000 ± 1000				

Note. ^a Corrected for time dilation.

present several problems in interpreting the explosion. The enormous luminosity at peak cannot be powered by radioactive ⁵⁶Ni (Pastorello et al. 2010; Quimby et al. 2011b; Chomiuk et al. 2011; Leloudas et al. 2012) which is the canonical energy source for SNe Ic emission. However, we showed in Section 4 that the tail phase luminosity in some objects declines in a similar fashion as to what would be expected from ⁵⁶Co decay.

In the following subsections we use this most extensive data set to constrain plausible models for the origin of these SNe, particularly using the bolometric luminosity from -30 to 200 days and the temperature and velocity information. In this paper, we focus on quantitative modeling of the magnetar spin-down scenario (Section 6.2). Several other models have been proposed, which we briefly review in Section 6.1. The bolometric light curves used in this section are corrected for flux missed in both UV and NIR as described in Section 4.

6.1. Alternative Models

Alternative models have been proposed: the spin down of a rapidly rotating young magnetar (Kasen & Bildsten 2010; Woosley 2010; Dessart et al. 2012); interaction of the SN ejecta with a massive ($3-5 M_{\odot}$) C/O-rich CSM (Blinnikov & Sorokina 2010); shock breakout from dense mass loss (Chevalier & Irwin 2011); or pulsational pair instability in which collisions between high-velocity shells are the source of multiple, bright optical transients (Woosley et al. 2007).

The first scenario considered is the pulsational pair-instability model, where the luminosity is powered by the collision of shells of material ejected at different times by the pulsations (see Chatzopoulos & Wheeler 2012 for the implementation of this on

SL-SNe Ic). The outbursts are expected to be energetic, reaching very high peak luminosities and creating hot ($T_{\text{eff}} \approx 25,000$ K), optically thick photospheres (Woosley et al. 2007). PS1 has occasionally observed the explosion sites of the five SL-SNe presented here, and SN 2010gx on 3–5 occasions (per event) in one of $g_{\text{P1}}r_{\text{P1}}i_{\text{P1}}z_{\text{P1}}y_{\text{P1}}$ filters, reaching typical AB magnitudes of 22, 21.6, 21.7, 21.4, and 19.3 (see Section 2). This would correspond to absolute magnitudes of roughly -16 to -19 . We found no detection of any previous outburst to these magnitude limits in the 1–2 yr periods before explosion. Typically there were 5–10 epochs of images from PS1. This is not a constant monitoring period, and it does not rule out that pre-explosion outbursts occur, but we have found no evidence for them.

The second scenario is that of circumstellar interaction proposed by Chevalier & Irwin (2011) in which the interaction between the ejecta and the CSM converts the ejecta’s kinetic energy into radiation. This requires the diffusion radius of the SN to be about the radius of the stellar wind expelled by the SN progenitor. Based on this model of Chevalier & Irwin (2011), Chomiuk et al. (2011) determined the dense wind and ejecta parameters for the observed $z \simeq 1$ SL-SNe. This requires a mass-loss rate of $6 M_{\odot}$ in the last year before the SN explosion, with an outer radius of around $40,000 R_{\odot}$, and ejecta mass of $10 M_{\odot}$ (consistent with the estimates reported in Moriya & Tominaga 2012). The rise times of our low- z SNe are similar to that of PS1-10awh (from Chomiuk et al. 2011)—around 10–30 days which would lead to similar estimates of masses. The detection of He I in SN 2012il at ~ 53 days is perhaps some hint that the dense CSM wind could be plausible, since it is difficult to find any known massive star example in the local universe

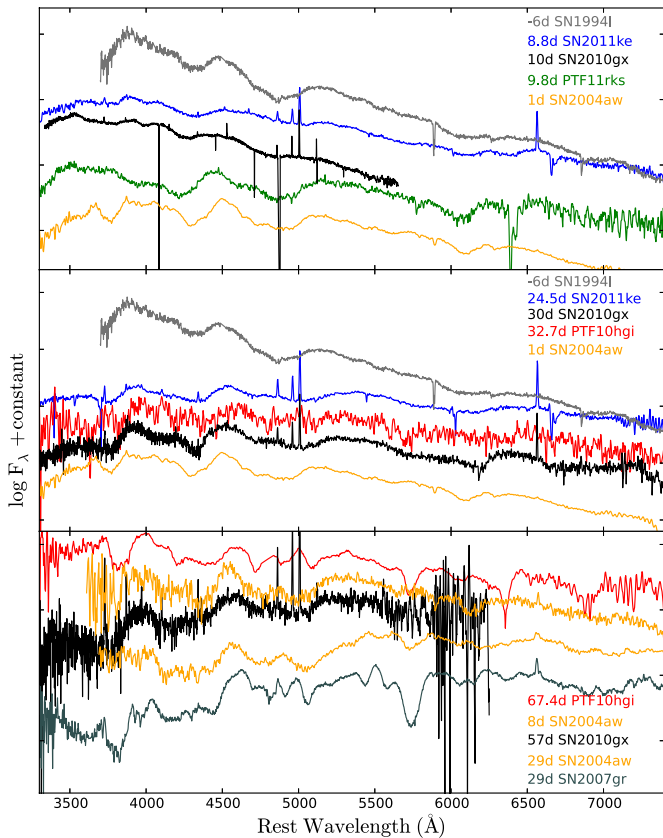


Figure 10. Top: comparison of early-time spectra of SN 2011ke and PTF11rks with that of SN 2010gx (Pastorello et al. 2010) and those of Type Ic SNe 2004aw (Taubenberger et al. 2006) and 1994I (Baron et al. 1996). At ~ 10 days post-maximum PTF11rks is already more developed than SN 2011ke and SN 2010gx. Middle: comparison at about ~ 30 days post-peak of the same objects as for the previous panel, but showing PTF11rks instead of PTF10hgi. Bottom: comparison of the spectrum of PTF10hgi at ~ 67 days with those of SN 2010gx at the pseudo-nebular phase, SN 2004aw at maximum light during the photospheric period, and Type Ic SN 2007gr (Valenti et al. 2008; Hunter et al. 2009). The spectrum of PTF10hgi is more similar to those of SNe 2004aw and 2007gr at 29 days rather than those of SN 2010gx at 57 days and SN 2004aw at 8 days (as noted in Pastorello et al. 2010).

(A color version of this figure is available in the online journal.)

which has a dense and extended wind comprising $6 M_{\odot}$ of C+O material only. Although the S/N in the NIR is low, the He I line is relatively broad, indicating that it arises from ejecta. Although most SL-SNe have similar rise times which are feasible in the diffusion model of Chevalier & Irwin (2011), the light curves of SN 2010gx (Pastorello et al. 2010), PTF11rks and SN 2012il are not symmetric, which one would expect in this dense wind scenario. However, Ginzburg & Balberg (2012) showed as the rise and fall times can be different. They also showed that the tail phase can be explained as diffusion from the inner layers which can slow the decline. We have not investigated in this scenario in depth, but a combination of this model plus a ^{56}Ni tail would be unlikely because of the necessity of full γ -ray trapping (see Section 4).

A variant of the previous scenario was proposed by Blinnikov & Sorokina (2010) claiming high luminosities from a radiative shock in a massive C–O shell. The shells have radii and density profiles that are similar to the dense wind of Chevalier & Irwin (2011), with a density gradient of $\rho(r) \propto r^{-1.8}$ and radii of the order of $10^5 R_{\odot}$. Considering a total ejecta mass $M_{\text{ej}} \lesssim 1 M_{\odot}$, which collides with a shell of mass $5 M_{\odot}$, these models have initial energies ($2\text{--}4 \times 10^{51}$ erg) higher than those retrieved

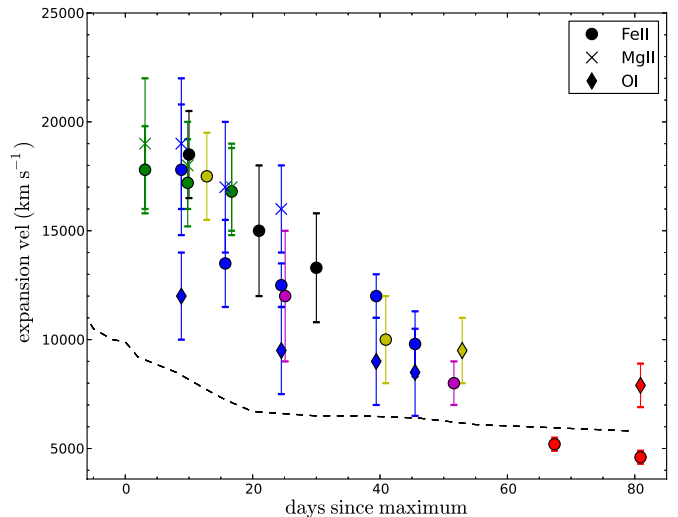


Figure 11. Expansion, photospheric velocity as measured from the different lines. Phases are relative to light curve peak. Measurements of PTF11rks (green), SN 2011ke (blue), SN 2012il (gold), PTF10hgi (red), and SN 2011kf (purple) are reported with those of SN 2010gx (black). The dashed black line shows the Fe II evolution in the normal Type Ic SN 2007gr.

(A color version of this figure is available in the online journal.)

by the expansion velocities during the pseudo-nebular phase in our set of spectra ($\sim 1 \times 10^{51}$ erg). Moreover, the light curves are too shallow and they are not able to reproduce the SN 2010gx decline after 30 days post-maximum light. We find no unequivocal signs of interaction in the spectra of the objects.

In Sections 3.1 and 4 we have presented detections of the SNe at later times than published to date, due to our focus on low-redshift candidates. We detect a flattening of the light curve and a tail phase in four out of five transients and this slope appears to be consistent with ^{56}Co decay. In summary, these interaction scenarios can reproduce the peak energy and diffusion time. However, the ejecta/shell velocity should be lower (by about a factor of two) than those observed. In addition, one still needs another power source for the late time luminosity that we now detect in these SL-SNe Ic.

As shown previously by Chatzopoulos et al. (2009), Pastorello et al. (2010), Quimby et al. (2011b), Chomiuk et al. (2011), Chatzopoulos et al. (2012), and Leloudas et al. (2012), the light curve peaks cannot be fit with a physically plausible ^{56}Ni diffusion model like normal SNe Ic, and our similarly shaped light curves result in the same conclusion. If the tail phase was actually due to ^{56}Co powering, then approximately $1\text{--}4 M_{\odot}$ of ^{56}Ni would be required, but this would not be enough to power the peak luminosity solely through radioactive heating. In Figure 12 we also show the best-fitting ^{56}Ni -powered models, under the assumptions that the ^{56}Ni mass must be $< 50\%$ ejecta mass, and that the ejecta velocities are less than $15,000 \text{ km s}^{-1}$. The first assumption is based on the implausibility of a pure ^{56}Ni ejecta; Umeda & Nomoto (2008) found typical ^{56}Ni masses which are at most 20% of the ejecta, while if the ejecta was comprised of more ^{56}Ni than this, we would expect to see spectra dominated by Fe-group rather than intermediate-mass elements. The velocity constraint is motivated by the observed velocities in our sample. Thus we derived kinetic energies of $6.2 \lesssim E(10^{51} \text{ erg}) \lesssim 15.0$, ejecta masses of $5.9 \lesssim M_{\text{ej}}(M_{\odot}) \lesssim 13.0$, and ^{56}Ni masses of $2.9 \lesssim M_{^{56}\text{Ni}}(M_{\odot}) \lesssim 6.0$ (see Appendix D.5 for further details).

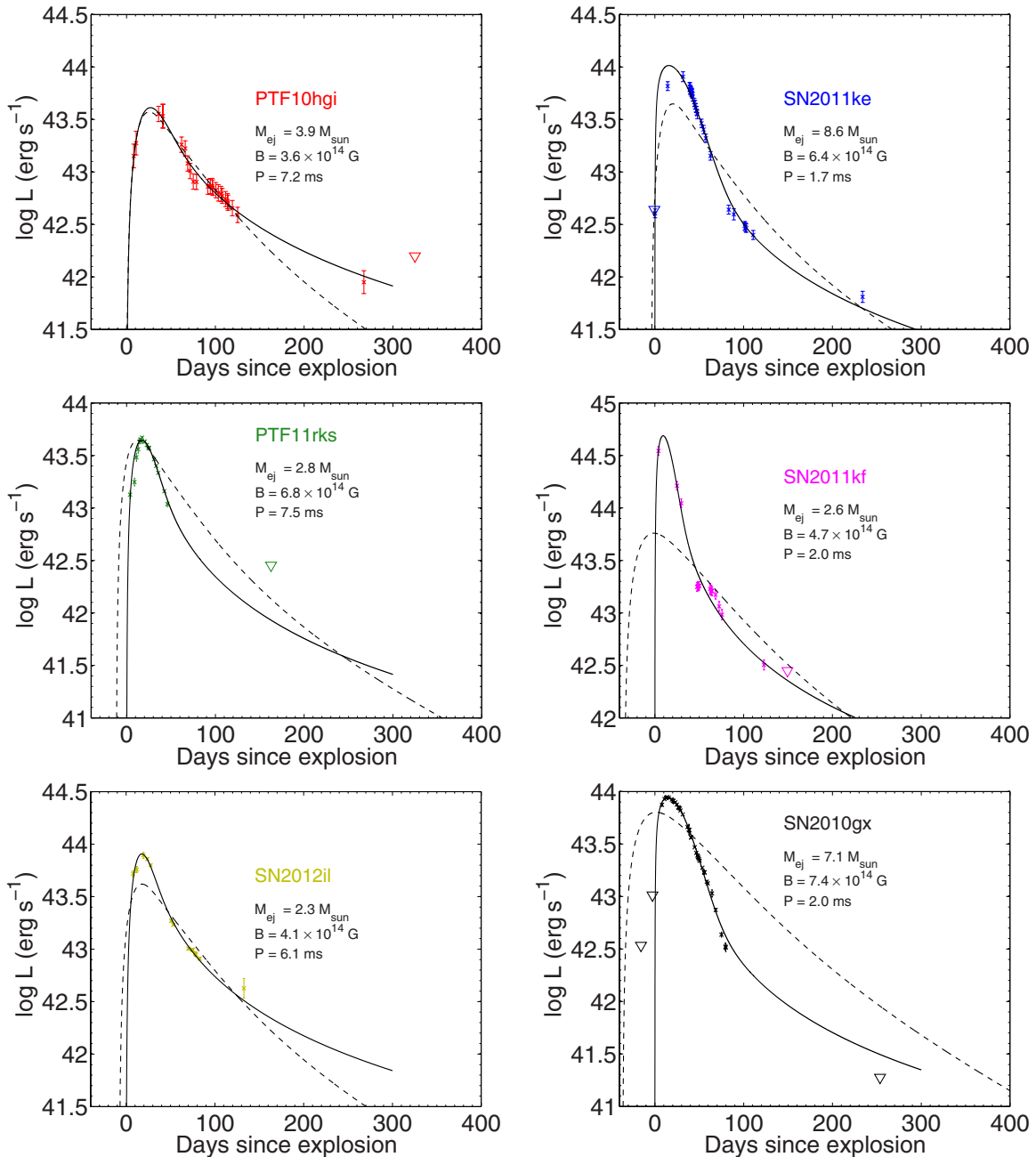


Figure 12. Bolometric light curves of PTF10hgi, SN 2011ke, PTF11rks, SN 2011kf, SN 2012il, and SN 2010gx and the diffusion semi-analytical model that best fits the light curve (black solid line). The limits are shown as empty upside down triangles. The best fit of the ^{56}Ni model (black dashed line) for each SN is also reported. (A color version of this figure is available in the online journal.)

From the fits, it appears that no physical and consistent solutions for ^{56}Ni heating can be determined, as found by previous authors (Pastorello et al. 2010; Quimby et al. 2011b; Chomiuk et al. 2011; Leloudas et al. 2012). One could invoke a combination of CSM interaction to explain the peak luminosity and then ^{56}Ni masses of 1–4 M_{\odot} to account for the tail phases, but, as discussed above, this requires full γ -ray trapping and somewhat fine tuning of the two scenarios to work in unison.

6.2. Magnetar Model

Kasen & Bildsten (2010), Woosley (2010), and Dessart et al. (2012) have already proposed that a rapidly spinning magnetar can deposit its rotational energy into an SN explosion and significantly enhance the luminosity. This appears to be an

appealing scenario as the model is fairly simple, and this additional power source can potentially transform a canonical Type Ic SN into an SL-SN Ic. To investigate this further and quantitatively compare our extensive light curves with this model, we have derived semi-analytical diffusion models. We use standard diffusion equations derived by Arnett (1982) and add magnetar powering (as in Kasen & Bildsten 2010) to fit the light curves of our five objects. A full description can be found in Appendix D. Assuming full trapping of the magnetar radiation,¹⁸ the ejecta mass M_{ej} , explosion energy E_k , and the opacity κ only influence the bolometric light curve through

¹⁸ Which is the case if the SED of the magnetar is dominated by X-ray radiation, as in the Crab pulsar, for instance (Weisskopf et al. 2000).

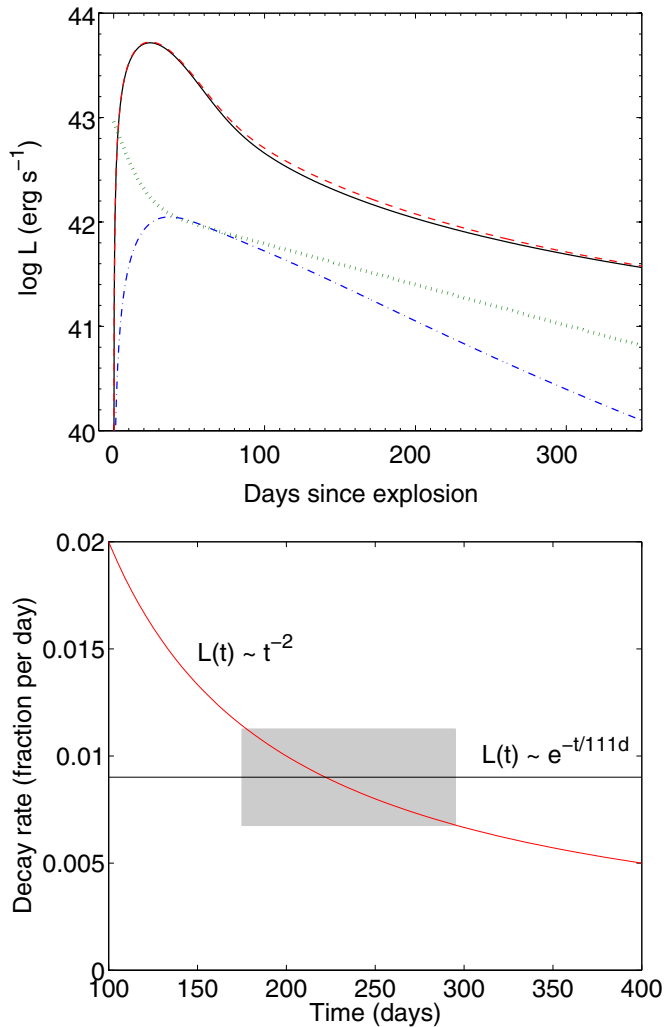


Figure 13. Top: bolometric light curves for $B_{14} = 5$, $P_{\text{ms}} = 5$, $M_{\text{ej}} = 5 M_{\odot}$ without ^{56}Ni contribution (black solid) and with $M(^{56}\text{Ni}) = 0.1 M_{\odot}$ (red dashed). Also shown is the total energy emitted by $M(^{56}\text{Ni}) = 0.1 M_{\odot}$ (green dotted) and the light curve produced by this amount of ^{56}Ni in a $5 M_{\odot}$ ejecta with $E_{\text{k}} = 10^{51}$ erg (blue dot-dashed). Bottom: comparison between magnetar and ^{56}Co decay rate. The gray box is the region where the two slopes are similar to within 25%.

(A color version of this figure is available in the online journal.)

their combined effect on the diffusion timescale parameter (see Appendix D):

$$\tau_{\text{m}} = 10 \text{ d} \left(\frac{M_{\text{ej}}}{1 M_{\odot}} \right)^{3/4} \left(\frac{E_{\text{k}}}{10^{51} \text{ erg}} \right)^{-1/4} \left(\frac{\kappa}{0.1 \text{ cm}^2 \text{ g}^{-1}} \right)^{1/2}. \quad (2)$$

The magnetar luminosity depends on two parameters, the magnetic field strength B_{14} (expressed in terms of 10^{14} G) and the initial spin period P_{ms} (in milliseconds). Combined with the explosion date t_0 , we therefore have four free parameters to fit. Table 4 lists the best-fit parameters for each object, and Figure 12 shows the fits. As the χ^2 fitting gives good matches to models *without* ^{56}Ni , we have no need to introduce ^{56}Ni as an additional free parameter. All the models have $M(^{56}\text{Ni}) = 0 M_{\odot}$ and we investigated the sensitivity to the assumed ^{56}Ni mass by recomputing the fits including $0.1 M_{\odot}$ of ^{56}Ni in the ejecta (the typical ^{56}Ni yield in core-collapse SNe). We find virtually the same fit parameters as we do without the nickel. As can be seen from Figure 13 (top), the two magnetar models

Table 4

Best-fit Parameters for Magnetar Modeling of the Bolometric Light Curves and χ_{red}^2 Value on the Left; Derived Parameters on the Right

Object	τ_{m} (days)	B_{14}	P_{ms}	t_0 (MJD)	χ_{red}^2	E^{mag} (10^{51} erg)	M_{ej} (M_{\odot})	$V_{\text{core}}^{\text{final}}$ (km s^{-1})
SN 2011ke	35.0	6.4	1.7	55650.65	1.8	6.9	8.6	12400
SN 2011kf	15.4	4.7	2.0	55920.65	5.8	5.0	2.6	19600
SN 2012il	18.4	4.1	6.1	55918.56	3.9	0.5	2.3	10500
PTF10hgi	26.2	3.6	7.2	55322.78	0.5	0.4	3.9	7700
PTF11rks	21.0	6.8	7.5	55912.11	5.0	3.6	2.8	16500
SN 2010gx	32.4	7.4	2.0	55269.22	3.9	5.0	7.1	11900

($B_{14} = 5$, $P_{\text{ms}} = 5$, $M_{\text{ej}} = 5 M_{\odot}$) with (red dashed) and without ^{56}Ni (black solid) are similar. The late decline rate in the magnetar model (> 100 days) is actually quite similar to the ^{56}Co decay rate as shown in Figure 13 (bottom), but fully trapped γ -rays are required. As Figure 13 shows, this full trapping is different from the typical light curve of a radioactivity-powered Type Ib/c SN in which full trapping is not observed. Recently, Dexter & Kasen (2012) showed that fall-back accretion can give a similar asymptotic behavior of the light curve ($L_{\text{t}} \propto t^{-5/3}$) which is a scenario that would need further investigation.

The light curves are quite well reproduced with appropriate choices of parameters, and the tail phase luminosities that we measure can also be explained with this model. The diffusion timescale parameters are between 15 and 35 days, which corresponds to ejecta masses of 2–9 M_{\odot} for $\kappa = 0.1 \text{ cm}^2 \text{ g}^{-1}$ (see Appendix D for further details about κ) and

$$E_{\text{k}} = 10^{51} + \frac{1}{2}(E^{\text{mag}} - E^{\text{rad}}) \text{ (erg)}, \quad (3)$$

where E^{mag} is the total energy of the magnetar and E^{rad} is the total radiated energy of the SN. We use a factor of 1/2 for an approximation of the average kinetic energy over the magnetar energy input phase, which we show in Appendix D.4 produces good agreement with more detailed time-dependent calculations of E_{k} .¹⁹ These ejecta masses are consistent with the ones derived for radioactivity-powered Type Ib/c ejecta (Ensmann & Woosley 1988; Shigeyama et al. 1990; Valenti et al. 2011; Drout et al. 2011; Eldridge et al. 2013). Furthermore, Figure 14 shows that the evolution of photospheric velocities and temperatures match the observed ones reasonably well. While the velocity and temperature evolution as estimated from our models are crude, this good agreement is an important test for the physical self-consistency of the model. From the light curve fits to ejecta mass and kinetic energy, we estimate the ejecta velocities (V_{core} ; see Equation (D11)) which we compare to the observed velocities of the emission lines (Ca H&K and Mg I] $\lambda 4571$; see Table 3), finding them reasonably similar.

From the plot of bolometric light curves shown in Figure 6, it appears that there is a gap between the faintest SL-SNe Ic and the brightest normal Type Ic. One possibility is that this is an observational bias. As SL-SNe Ic are intrinsically rare (Quimby et al. 2011b), we find them at moderate redshifts simply due to the large survey volume required to find them. If intermediate objects were also as rare, then we would require wider field searches to encompass more local volume as they

¹⁹ We also investigated the sensitivity to this assumption by computing masses (as well as photospheric velocities and temperatures) also from $E_{\text{k}} = 10^{51} + 0.4E^{\text{mag}}$ where the 40% conversion to kinetic energy is a typical value (Woosley 2010). We found very small differences in the derived quantities.

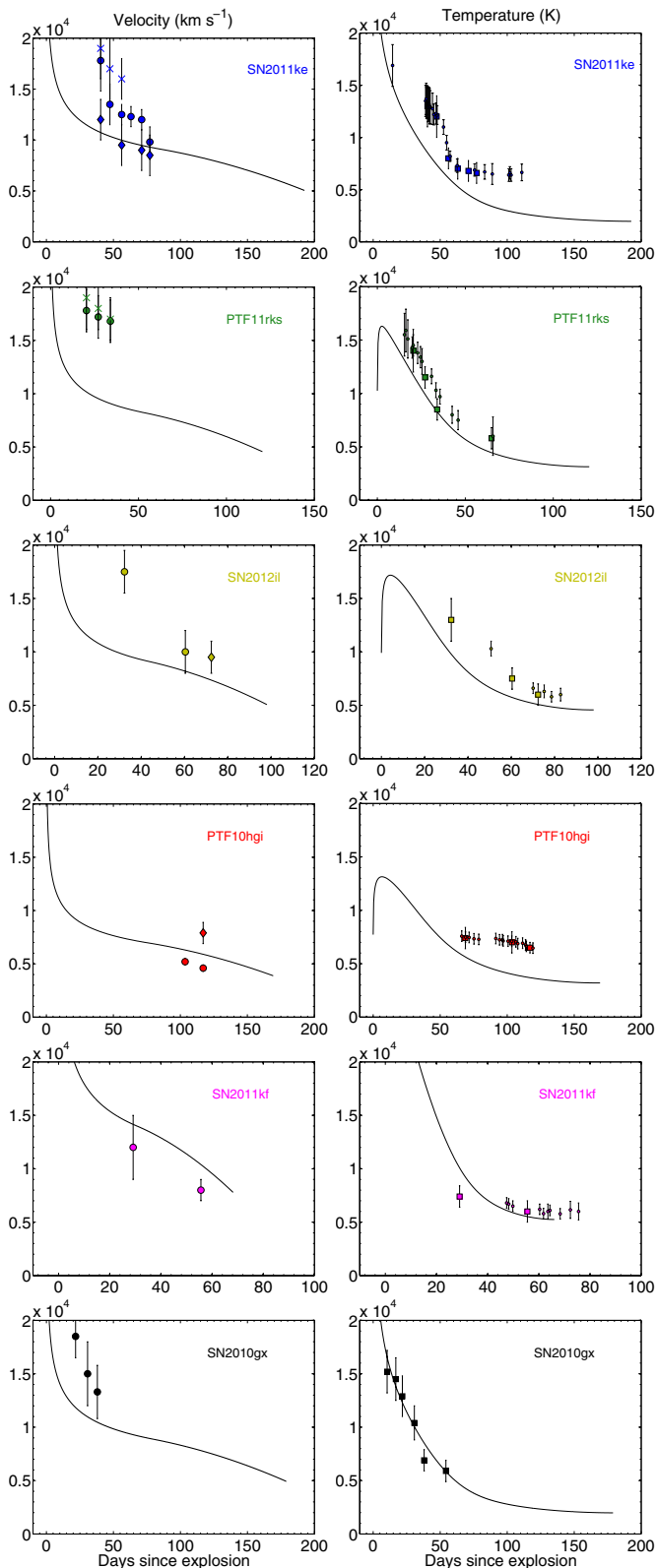


Figure 14. Left: photospheric velocities of SN 2011ke, PTF11rks, SN 2012il, PTF10hgi, SN 2011kf, SN 2010gx, and their values in the semi-analytical models best fitting the light curve data. Different symbols correspond to different ions as in Figure 11. Right: temperature evolution of SN 2011ke, PTF11rks, SN 2012il, PTF10hgi, SN 2011kf, SN 2010gx, and their values in the semi-analytical models best fitting the light curve data.

(A color version of this figure is available in the online journal.)

may evade detection at the higher redshifts of known population of SL-SNe. An alternative explanation is that the mechanism powering the SL-SNe has a minimum energy. From the semi-analytic magnetar model of Kasen & Bildsten (2010), which we have used to match our light curves, we see that the peak magnetar luminosity is inversely proportional to the square of the magnetic field (Equation (4) of Kasen & Bildsten 2010). Hence, the question arises, could the apparent lower luminosity limit to the SL-SNe Ic be caused by some physical upper limit to the magnetic field in a magnetar? For our faintest SL-SNe, and using a minimum plausible ejecta mass of $1 M_{\odot}$, we determine an upper limit to the magnetar B -field of $B < 1.4 \times 10^{15}$ G from Equation (4) of Kasen & Bildsten (2010). If we consider that Kasen & Bildsten (2010) assume an angle between the B field and the spin axis of the magnetar of 45° , then a factor of two higher than this value could be a plausible maximum. We hence adopt $B < 3 \times 10^{15}$ G.

The most conservative limit we can set is that the magnetic energy in the magnetar must be less than the gravitational binding energy of the neutron star (Chandrasekhar & Fermi 1953). This implies that

$$B < 10^{18} \left(\frac{M_{\text{NS}}}{1.4 M_{\odot}} \right) \left(\frac{R_{\text{NS}}}{10 \text{ km}} \right)^{-2} \text{ G} \quad (4)$$

which does not set a particularly stringent upper limit on the B -field. This limit is consistent with the B values retrieved from all the galactic magnetars studied so far which have $B \sim 10^{14}$ – 10^{15} G (Woods & Thompson 2006). However, magnetic fields are known to be a possible source of braking in stars (Meynet et al. 2011), while the magnetar models require an extreme magnetic field and fast rotational period. An explanation for both a small rotational period and a large magnetic field could be a large-scale helical dynamo that is possible when the rotation period is comparable to the timescale of the convective motions (Duncan & Thompson 1992).

7. CONCLUSION

We have presented extensive photometric and spectroscopic coverage of five of the lowest redshift SL-SNe Ic. For 1 of them, SN 2011ke, we present a light curve from -30 days to 200 days, showing a well-constrained rise time and a clear detection at 200 days indicating a flattening of the luminosity. In four out of six SL-SNe, we show that there is significant luminosity in this late tail phase, and we illustrate that these measurements can aid our understanding of the power source and the possible progenitors of these ultra-luminous transients.

The five SNe, namely PTF10hgi, SN 2011ke, PTF11rks, SN 2011kf, and SN 2010gx, have absolute magnitudes $-21.73 \lesssim M_g(\text{mag}) \lesssim -20.42$ similar to previous SL-SNe as well as a spectral evolution resembling SN 2010gx (Pastorello et al. 2010). There is some variation in the sample as two of the objects are fainter than the rest and spectroscopically evolve faster. PTF10hgi and PTF11rks have peak absolute magnitudes fainter than $M_g > -21$ mag. The spectra of PTF11rks evolves faster than the rest and at 10 days post-maximum it resembles a normal Type Ic at peak. In contrast, SN 2010gx and 3 other SNe presented here typically take 30 days to evolve to this phase. The latest spectrum we have of PTF10hgi shows well-developed lines of Fe II at velocities which are more comparable with standard Type Ic SNe, significantly slower than the bulk of the SL-SNe Ic sample. Our *xshooter* spectrum of SN 2012il +52 days is the only NIR spectrum of SL-SNe Ic

and we detect a broad He I λ 10830 in emission implying that at least some SL-SNe Ic are not completely He-free. During the epochs of ± 10 days around peak the temperatures and velocities are nearly constant and do not show a clear decrease until after that period. We find that the decay timescale in the 100–200 day period is similar to that expected from the radioactive decay of ^{56}Co , but it requires the γ -rays to be fully trapped. This is in contrast to the faster decline observed in most Type Ib/c SNe, where γ -ray leakage has a significant effect from 50 days onward (Sollerman et al. 2000). Hence it is unlikely that this is due to large amounts ($1\text{--}4 M_{\odot}$) of ^{56}Ni produced in the explosion.

We applied a semi-analytical diffusion model with energy input from a spinning down magnetar to fit the light curves of our five objects and SN 2010gx, including the diffusion peak and the tail phase detections. All light curves including the tail phases are reproduced with feasible physical values for a magnetar-powered SL-SN. We require $3.6 \lesssim B_{14} \lesssim 7.4$, $1.7 \lesssim P_{\text{ms}} \lesssim 7.5$ consistent with B of known galactic magnetars ($B_{14} \sim 1\text{--}10$) and with physically plausible periods ($P_{\text{ms}} > 1$). We derived energies of $0.4 \lesssim E^{\text{mag}} (10^{51} \text{ erg}) \lesssim 6.9$ and ejected masses of $2.3 \lesssim M_{\text{ej}} (M_{\odot}) \lesssim 8.6$.

The well-sampled data of the five SL-SNe Ic presented here combined with those of SN 2010gx point toward an SN explosion driven by a magnetar as a viable explanation for all the SL-SNe Ic. The light curves are reproduced and the model temperatures and velocities are in reasonable agreement with the observational data. However even if this is a reliable model, it still leaves other open questions, such as the following.

1. Do H-rich SNe powered by magnetars exist?²⁰ Possibly SN 2008es (Gezari et al. 2009) could be an example of such a luminous Type II SN. In other words, why do we observe so many more H-free than H-rich SL-SNe?
2. What is the role of metallicity in the progenitor stars evolution that will produce H-free SL-SNe? It appears that they are all associated with faint dwarf galaxies and almost certainly low-metallicity progenitors.
3. Do realistic spectral calculations of magnetar-driven SN reproduce the main observed features at late time?
4. Where is the peak of the magnetar SED and how does the magnetar radiation deposit and thermalize in the nebular phase?

To address these, further observations are required combined with modeling. Theoretical modeling of high-quality data in the nebular phase to determine the ejecta masses, composition and the mass of ^{56}Co contributing to the luminosity seems the most likely way to make progress. Optical spectroscopy at ~ 300 days post-explosion appears to us to be the next step in probing the nature of these events. At $z \sim 0.1$, the typical AB magnitudes of these sources are $\sim 23 \pm 0.5$, requiring approximately one night of 8 m telescope time to gather a spectrum with high enough S/N to measure the expected Ic-like emission lines with confidence.

We thank Dan Kasen for providing us with the data of the simulations of Kasen & Bildsten (2010) in order to compare them with the output of our code. The research leading to these results has received funding from the European Research Council under the European Union’s Seventh Framework Programme (FP7/2007-2013)/ERC Grant agreement No. [291222]

²⁰ Some studies, in order to investigate the existence of H-rich SNe powered by magnetar, have been done by Barkov & Komissarov (2011).

(PI: S. J. Smartt). A.P., S.B., and M.T.B. are partially supported by the PRIN-INAF 2011 with the project “Transient Universe: from ESO Large to PESSTO.” G.L. is supported by the Swedish Research Council through grant No. 623-2011-7117. J.P.U.F. acknowledges support from the ERC-StG grant EGG-278202. The Dark Cosmology Centre is funded by the DNRF. S.T. acknowledges support by the TRR 33 “The Dark universe” of the German Research Foundation. The Pan-STARRS1 Surveys (PS1) have been made possible through contributions of the Institute for Astronomy, the University of Hawaii, the Pan-STARRS Project Office, the Max-Planck Society and its participating institutes, the Max Planck Institute for Astronomy, Heidelberg and the Max Planck Institute for Extraterrestrial Physics, Garching, The Johns Hopkins University, Durham University, the University of Edinburgh, Queen’s University Belfast, the Harvard-Smithsonian Center for Astrophysics, the Las Cumbres Observatory Global Telescope Network Incorporated, the National Central University of Taiwan, the Space Telescope Science Institute, the National Aeronautics and Space Administration under grant No. NNX08AR22G issued through the Planetary Science Division of the NASA Science Mission Directorate, the National Science Foundation under grant No. AST-1238877, and the University of Maryland. We greatly appreciate the work of the support astronomers at the Telescopio Nazionale Galileo, the Copernico Telescope, the 2.2 m Telescope at Calar Alto, the Liverpool Telescope, the Nordic Optical Telescope, the New Technology Telescope, the William Herschel Telescope, the Faulkes Telescope North and the Gemini North. Funding for SDSS-III has been provided by the Alfred P. Sloan Foundation, the Participating Institutions, the National Science Foundation, and the U.S. Department of Energy Office of Science. The SDSS-III Web site is <http://www.sdss3.org/>.

Facilities: PS1, ING:Herschel, TNG, Gemini:Gillett, Asiago:Copernico, NTT, Liverpool:2m, NOT, CAO:2.2m, FTN

APPENDIX A

TABLES

In this Appendix the magnitudes of the 5 SNe presented in the main text are reported.

APPENDIX B

SEQUENCE STARS FOR PTF10hgi

Here we report the average magnitudes of the local sequence stars of PTF10hgi used to calibrate the photometric zero points for non-photometric nights. They are reported in Table A8 along with their rms (in parentheses). Their positions are marked in Figure 15, along with the SN position.

APPENDIX C

SPECTRAL EVOLUTION

A binned spectral evolution of the SL-SNe discussed in the main text is reported here (see Figure 16).

APPENDIX D

MAGNETAR-POWERED LIGHT CURVES

Arnett (1982) derived the solution for the bolometric light curve of a homologously expanding ejecta subject to a total

Table A1
Observed (Non-*K*-corrected) Photometry of PTF10hgi Plus Associated Errors in Parentheses

Date	MJD	Phase ^a	<i>u</i>	<i>g</i>	<i>r</i>	<i>i</i>	<i>z</i>	Telescope
2010 May 15	55331.61	−28.0			19.10 (−)			ATel 2740
2010 May 18	55334.57	−25.3			18.90 (0.07)			PS1
2010 May 26	55342.33	−18.2				18.49 (0.07)		PS1
2010 May 26	55342.34	−18.2				18.48 (0.06)		PS1
2010 Jun 15	55362.40	0.0		18.23 (0.05)				PS1
2010 Jun 19	55366.45	3.7			18.04 (0.10)			PS1
2010 Jun 20	55367.75	4.9			18.00 (−)			ATel 2740
2010 Jun 21	55368.53	5.4				18.01 (0.05)		PS1
2010 Jun 21	55368.55	5.4				18.02 (0.05)		PS1
2010 Jul 13	55390.81	25.8	20.08 (0.12)					UVOT
2010 Jul 17	55395.39	30.0		18.93 (0.05)	18.63 (0.08)	18.56 (0.05)	18.58 (0.14)	LT
2010 Jul 18	55396.00	30.5	20.80 (0.15)					UVOT
2010 Jul 20	55398.47	32.8		19.24 (0.08)	18.88 (0.09)	18.84 (0.08)	18.91 (0.10)	LT
2010 Jul 23	55401.50	35.5		19.44 (0.08)	19.11 (0.09)	18.91 (0.08)	19.10 (0.10)	LT
2010 Jul 27	55405.39	39.1		19.60 (0.05)	19.17 (0.06)	19.03 (0.03)	19.16 (0.10)	LT
2010 Jul 31	55409.40	42.7		19.74 (0.02)	19.29 (0.03)	19.10 (0.04)	19.24 (0.10)	LT
2010 Aug 14	55423.39	55.4		20.16 (0.03)	19.59 (0.03)	19.44 (0.04)	19.30 (0.10)	LT
2010 Aug 17	55426.42	58.2		20.21 (0.04)	19.60 (0.05)	19.47 (0.05)	19.34 (0.11)	LT
2010 Aug 19	55428.87	60.4		20.28 (0.17)	19.64 (0.07)	19.52 (0.05)	19.37 (0.09)	FTN
2010 Aug 20	55429.43	60.9		20.33 (0.13)	19.66 (0.06)	19.53 (0.06)	19.39 (0.16)	LT
2010 Aug 24	55433.38	64.5		20.40 (0.07)	19.70 (0.05)	19.60 (0.07)	19.40 (0.05)	LT
2010 Aug 27	55436.40	67.3		20.48 (0.29)	19.77 (0.12)	19.62 (0.09)	19.44 (0.26)	LT
2010 Aug 30	55439.82	70.4		20.49 (0.08)	19.83 (0.04)	19.64 (0.03)	19.48 (0.09)	FTN
2010 Sep 1	55441.37	71.8		20.54 (0.01)	19.84 (0.04)	19.71 (0.05)	19.56 (0.05)	LT
2010 Sep 5	55445.37	75.4		20.64 (0.04)	19.89 (0.04)	19.76 (0.06)	19.65 (0.07)	LT
2010 Sep 7	55447.80	77.6		20.67 (0.03)	19.92 (0.04)	19.82 (0.03)	19.78 (0.07)	FTN
2010 Sep 8	55448.38	78.2		20.70 (0.03)	19.97 (0.04)	19.87 (0.04)	19.83 (0.08)	LT
2010 Sep 13	55453.77	83.1		20.85 (0.05)	20.06 (0.05)	19.97 (0.05)	20.04 (0.09)	FTN
2010 Sep 20	55460.36	89.0		21.01 (0.08) ^b	20.21 (0.09) ^b		20.21 (0.13) ^b	LT
2011 Feb 22	55615.21	229.8				23.82 (0.31) ^b		WHT
2011 Feb 24	55616.23	231.2			23.92 (0.30) ^b			WHT
2011 Apr 28	55679.56	288.3		>21.98				PS1
<i>Host</i>								
2012 May 26	56073.00	646.0		23.64 (0.23)	22.01 (0.09)			WHT
2012 May 28	56075.00	648.0				22.18 (0.15)	21.59 (0.15)	TNG

Notes. Also reported are the host galaxy magnitudes, measured after the SN has faded. PS1 = 1.8 m Pan-STARRS1; UVOT = *Swift* + UVOT; LT = 2.0 m Liverpool Telescope + RATCam; FTN = 2.0 m Faulkes Telescope North + MEROPE; WHT = 4.2 m William Herschel Telescope + ACAM.

^a Phase with respect to the *g*-band maximum, corrected for time dilation.

^b Magnitudes after image subtraction using 646–648 day images.

(absorbed) power $P(t)$ as

$$L_{\text{SN}}(t) = e^{-(t/\tau_m)^2} \int_0^{t/\tau_m} P(t') 2(t'/\tau_m) e^{(t'/\tau_m)^2} \frac{dt'}{\tau_m} \text{ erg s}^{-1}, \quad (\text{D1})$$

where τ_m is the diffusion timescale parameter, which in the case of uniform density ($E_k = (3/10)M_{\text{ej}}V_{\text{ej}}^2$) is

$$\tau_m = \frac{1.05}{(\beta c)^{1/2}} \kappa^{1/2} M_{\text{ej}}^{3/4} E_k^{-1/4} \text{ s}. \quad (\text{D2})$$

The parameter β has a typical value of 13.7 (Arnett 1982), which we use throughout. Apart from spherical symmetry and homology, the Arnett solution assumes a radiation pressure dominated gas, energy transport by diffusion, constant and gray opacity, and that the spatial distribution of energy input by the power source is proportional to the radiation energy density. The last assumption is for most cases the coarsest one, but the solutions are not critically dependent on deviations from it (Arnett 1982).

The power function $P(t)$ can generally be expressed as a sum of a set of source luminosities $L_i(t)$ multiplied by deposition

functions $D_i(t)$:

$$P(t) = \sum L_i(t) D_i(t) \text{ erg s}^{-1}. \quad (\text{D3})$$

For radioactivity from ^{56}Ni and its daughter nucleus ^{56}Co , the luminosity functions are

$$L_{^{56}\text{Ni}}(t) = 7.8 \times 10^{43} \left(\frac{M_{^{56}\text{Ni}}}{1 M_{\odot}} \right) e^{-t/\tau_{^{56}\text{Ni}}} \text{ erg s}^{-1}, \quad (\text{D4})$$

$$L_{^{56}\text{Co}}(t) = 1.4 \times 10^{43} \left(\frac{M_{^{56}\text{Ni}}}{1 M_{\odot}} \right) \frac{e^{-t/\tau_{^{56}\text{Co}}} - e^{-t/\tau_{^{56}\text{Ni}}}}{1 - \frac{\tau_{^{56}\text{Ni}}}{\tau_{^{56}\text{Co}}}} \text{ erg s}^{-1}, \quad (\text{D5})$$

where $M_{^{56}\text{Ni}}$ is the amount of ^{56}Ni formed in the explosion, and $\tau_{^{56}\text{Ni}}$ and $\tau_{^{56}\text{Co}}$ are the decay times of the isotopes (8.7 and 111 days, respectively).

For a magnetar with a 45° angle between the magnetic axis and spin axis, the dipole spin-down luminosity is (Ostriker & Gunn 1971; Kasen & Bildsten 2010)

$$L_{\text{magnetar}}(t) = 4.9 \times 10^{46} B_{14}^2 P_{\text{ms}}^{-4} \frac{1}{(1 + t/\tau_p)^2} \text{ erg s}^{-1}, \quad (\text{D6})$$

Table A2
Observed (Non-*K*-corrected) Photometry of SN 2011ke and Associated Errors in Parentheses, Plus Host (see Table A1)

Date	MJD	Phase ^a	<i>u</i>	<i>B</i>	<i>g</i>	<i>V</i>	<i>r</i>	<i>i</i>	<i>z</i>	Tel.
2011 Mar 16	55637.00	-43.3				>20.10				CSS
2011 Mar 30	55649.55	-32.3					>21.17			PS1
2011 Mar 30	55650.50	-31.5			21.00 (-)					ATel
2011 Mar 31	55651.58	-30.5						20.07 (0.06)		PS1
2011 Mar 31	55651.60	-30.5						20.05 (0.06)		PS1
2011 Apr 2	55653.57	-28.8					19.40 (0.05)			PS1
2011 Apr 2	55653.58	-28.8					19.41 (0.05)			PS1
2011 Apr 6	55657.99	-24.9				18.61 (0.08)				CSS
2011 Apr 14	55665.98	-17.9				18.06 (0.07)				CSS
2011 Apr 15	55666.80	-17.2			18.07 (0.08)		18.00 (0.06)	18.21 (0.08)		PS1
2011 Apr 25	55677.00	-8.3				17.65 (0.07)				CSS
2011 May 5	55686.50	0.0			17.70 (-)					ATel
2011 May 12	55693.98	6.5				17.75 (0.06)				CSS
2011 May 13	55694.99	7.4			18.08 (0.08)		17.91 (0.06)	18.15 (0.06)	18.20 (0.09)	LT
2011 May 13	55695.54	7.9	18.34 (0.11)		18.08 (0.04)		17.92 (0.02)	18.10 (0.04)	18.13 (0.05)	FTN
2011 May 15	55695.92	8.2		18.26 (0.09)		17.97 (0.08)				EKAR
2011 May 14	55695.92	8.2			18.15 (0.08)		18.01 (0.10)	18.15 (0.09)	18.22 (0.12)	LT
2011 May 14	55695.95	8.3			18.16 (0.08)		18.02 (0.04)	18.18 (0.04)	18.18 (0.09)	LT
2011 May 14	55696.37	8.6	18.46 (0.20)							UVOT
2011 May 15	55696.93	9.1			18.20 (0.14)		18.01 (0.06)	18.28 (0.08)	18.25 (0.20)	LT
2011 May 16	55697.96	10.0	18.72 (0.17)		18.17 (0.05)		18.07 (0.06)	18.19 (0.03)	18.22 (0.04)	LT
2011 May 17	55698.36	10.4	18.79 (0.24)		18.15 (0.07)		18.06 (0.06)	18.17 (0.04)	18.28 (0.05)	FTN
2011 May 17	55698.95	10.9	18.95 (0.21)		18.29 (0.05)		18.05 (0.03)	18.26 (0.04)	18.16 (0.07)	LT
2011 May 18	55700.04	11.8		18.62 (0.13)		18.11 (0.05)				EKAR
2011 May 18	55700.05	11.8					18.10 (0.08)	18.25 (0.04)		LT
2011 May 19	55700.90	12.6				18.14 (0.05)				EKAR
2011 May 19	55700.94	12.6	19.08 (0.10)		18.41 (0.02)		18.18 (0.02)	18.26 (0.02)	18.35 (0.03)	LT
2011 May 20	55702.03	13.6	19.23 (0.10)		18.46 (0.02)		18.19 (0.02)	18.26 (0.03)	18.43 (0.04)	LT
2011 May 21	55702.97	14.4			18.54 (0.02)		18.22 (0.02)	18.31 (0.02)	18.37 (0.03)	LT
2011 May 22	55703.93	15.2	19.31 (0.07)		18.60 (0.02)		18.30 (0.03)	18.34 (0.02)	18.42 (0.03)	LT
2011 May 23	55704.92	16.1		18.94 (0.04)		18.35 (0.04)				EKAR
2011 May 23	55704.93	16.1	19.33 (0.07)		18.65 (0.02)		18.33 (0.02)	18.42 (0.02)	18.45 (0.03)	LT
2011 May 27	55708.95	19.6		19.20 (0.04)		18.55 (0.03)				EKAR
2011 May 27	55709.40	20.0				18.56 (0.07)				CSS
2011 May 28	55710.29	20.8	19.97 (0.03)		18.98 (0.04)		18.51 (0.02)	18.48 (0.03)	18.56 (0.06)	FTN
2011 May 30	55710.37	20.9	20.08 (0.30)							UVOT
2011 May 31	55712.94	23.1	20.08 (0.09)		19.13 (0.02)		18.60 (0.02)	18.61 (0.02)	18.62 (0.03)	LT
2011 May 31	55712.97	23.2		19.45 (0.03)		18.73 (0.02)				EKAR
2011 Jun 3	55715.93	25.7	20.25 (0.10)		19.30 (0.02)		18.77 (0.02)	18.71 (0.02)	18.70 (0.03)	LT
2011 Jun 6	55719.37	28.8	20.79 (0.41)							UVOT
2011 Jun 7	55719.98	29.3		20.03 (0.09)						EKAR
2011 Jun 9	55721.93	31.0	21.69 (0.44)		19.79 (0.05)		19.09 (0.04)	19.06 (0.03)	19.05 (0.06)	LT
2011 Jun 12	55724.50	33.2				19.25 (0.11)				CSS
2011 Jun 17	55730.00	38.1		20.55 (0.08)		19.61 (0.04)				EKAR
2011 Jun 24	55736.75	44.0	22.05 (0.12)	20.98 (0.06)		20.03 (0.04)	19.81 (0.04)	19.76 (0.05)		NTT
2011 Jun 28	55740.90	47.6		21.24 (0.08)		20.33 (0.08)				EKAR
2011 Jul 2	55745.33	51.5			21.40 (0.16) ^b		20.42 (0.07) ^b	20.07 (0.07) ^b	19.94 (0.08) ^b	FTN
2011 Jul 9	55751.93	57.2			21.95 (0.16) ^b		20.99 (0.30) ^b	20.84 (0.17) ^b	20.64 (0.25) ^b	LT
2011 Jul 13	55755.93	60.7		21.52 (0.24)		21.00 (0.27)				EKAR
2011 Jul 23	55765.94	69.5			22.15 (0.06) ^b		21.26 (0.06) ^b	21.02 (0.07) ^b	20.86 (0.14) ^b	LT
2011 Jul 24	55766.89	70.3			22.18 (0.08) ^b		21.28 (0.07) ^b	21.06 (0.07) ^b	20.88 (0.14) ^b	LT
2011 Jul 25	55767.90	71.2			22.20 (0.06) ^b		21.32 (0.06) ^b	21.08 (0.07) ^b	20.91 (0.12) ^b	LT
2011 Aug 3	55776.89	79.1			22.40 (0.11) ^b		21.48 (0.10) ^b	21.24 (0.08) ^b	21.07 (0.15) ^b	LT
2011 Dec 21	55917.74	202.3			23.95 (0.30) ^b		23.14 (0.24) ^b	22.50 (0.20) ^b	22.30 (0.23) ^b	WHT
<i>Host</i>										
2012 May 26	56073.50	338.6			21.18 (0.05)		20.72 (0.04)	20.47 (0.04)	20.90 (0.10)	WHT
2004 Jun 12	53169.22		21.54 (0.24)		21.20 (0.08)		20.71 (0.08)	20.59 (0.11)	21.30 (0.67)	SDSS DR9

Notes. CSS = 0.7 m Catalina Schmidt Telescope; PS1 = 1.8 m Pan-STARRS1; LT = 2.0 m Liverpool Telescope + RATCam; FTN = 2.0 m Faulkes Telescope North + MEROPE; UVOT = *Swift* + UVOT; EKAR = 1.8 m Copernico Telescope + AFOSC; WHT = 4.2 m William Herschel Telescope + ACAM, NTT = 3.6 m New Technology Telescope + EFOC2, ATel = ATel 3344.

^a Phase with respect to the *g*-band maximum, corrected for time dilation.

^b Magnitudes after image subtraction using 339 day images.

Table A3
Observed (Non-*K*-corrected) Photometry of PTF11rks and Associated Errors in Parentheses, Plus Host (see Table A1)

Date	MJD	Phase ^a	<i>u</i>	<i>g</i>	<i>r</i>	<i>i</i>	<i>z</i>	Telescope
2011 Dec 21	55916.70	−13.4			19.9 (−)			ATel 3841
2011 Dec 27	55922.70	−8.4			19.1 (−)			ATel 3841
2011 Dec 30	55925.24	−6.3	20.49 (0.12)					UVOT
2012 Jan 1	55927.56	−4.3	20.30 (0.11)					UVOT
2012 Jan 2	55929.42	−2.8		19.26 (0.09)	19.03 (0.20)			LT
2012 Jan 3	55930.42	−1.9		19.19 (0.06)	18.94 (0.04)	19.14 (0.04)	19.25 (0.27)	LT
2012 Jan 4	55931.34	−1.1		19.18 (0.04)	18.88 (0.03)	19.05 (0.08)	19.19 (0.24)	LT
2012 Jan 5	55931.85	−0.7	20.46 (0.10)					UVOT
2012 Jan 5	55932.72	0.0		19.13 (0.05)	18.87 (0.05)	19.01 (0.03)	19.14 (0.21)	FTN
2012 Jan 8	55935.73	2.5		19.22 (0.04)	18.96 (0.02)	18.99 (0.04)	19.06 (0.06)	FTN
2012 Jan 9	55936.40	3.1		19.23 (0.03)	18.97 (0.03)	19.00 (0.04)	19.06 (0.08)	LT
2012 Jan 10	55936.71	3.4	20.55 (0.10)					UVOT
2012 Jan 12	55939.32	5.6		19.30 (0.02)	19.03 (0.06)	18.97 (0.04)	19.03 (0.05)	LT
2012 Jan 14	55941.32	7.2		19.37 (0.04)	19.04 (0.03)	18.98 (0.05)	19.07 (0.28)	LT
2012 Jan 15	55941.51	7.4	20.93 (0.16)					UVOT
2012 Jan 15	55942.35	8.1		19.38 (0.02)	19.04 (0.03)	18.98 (0.04)	19.09 (0.09)	LT
2012 Jan 21	55948.75	13.5		19.65 (0.04)	19.19 (0.02)	19.08 (0.04)	19.10 (0.07)	FTN
2012 Jan 24	55951.73	16.0		19.79 (0.04)	19.28 (0.03)	19.17 (0.05)	19.16 (0.06)	FTN
2012 Jan 27	55954.44	18.3		19.93 (0.05)	19.41 (0.06)	19.22 (0.08)	19.17 (0.14)	LT
2012 Jan 29	55956.84	20.3			19.46 (0.21)			FTN
2012 Feb 4	55962.75	25.2		20.58 (0.14)	19.62 (0.04)	19.44 (0.03)	19.35 (0.03)	FTN
2012 Feb 8	55966.74	28.6		20.90 (0.20) ^b	20.04 (0.08) ^b	19.84 (0.13) ^b	19.71 (0.16) ^b	FTN
2012 Mar 3	55990.34	48.4			20.82 (0.15) ^b	20.55 (0.44) ^b		LT
2012 Jun 26	56105.26	145.3		>22.9	>22.4	>22.1		WHT
<i>Host</i>								
2012 Sep 22	56192.50	218.3		21.67 (0.07)	20.83 (0.05)			WHT
2009 Oct 16	55121.47		21.51 (0.32)	21.59 (0.11)	20.88 (0.10)	20.71 (0.14)	20.03 (0.29)	SDSS DR9

Notes. *Swift* *u*-band data have been converted to SDSS magnitudes. UVOT = *Swift* + UVOT; LT = 2.0 m Liverpool Telescope + RATCam; FTN = 2.0 m Faulkes Telescope North + MEROPE; WHT = 4.2 m William Herschel Telescope + ACAM; GS = 8.1 m Gemini South + GMOS.

^a Phase with respect to the *g*-band maximum, corrected for time dilation.

^b Magnitudes after image subtraction using 218 day images or SDSS *iz* images.

Table A4
Observed (Non-*K*-corrected) NIR Photometry of PTF11rks Plus Associated Errors in Parentheses

Date	MJD	Phase ^a	<i>J</i>	<i>H</i>	<i>K</i>	Telescope
2012 Feb 7	55965.84	29.1			18.86 (0.10)	NOT
2012 Feb 8	55966.88	30.0	19.31 (0.10)			NOT
2012 Feb 9	55967.83	30.9	19.32 (0.10)			NOT
2012 Feb 10	55968.84	31.8	19.42 (0.10)	19.41 (0.09)		NOT

Notes. NOT = 2.56 m Nordic Optical Telescope + NOTCam.

^a Phase with respect to the *g*-band maximum, corrected for time dilation.

where B_{14} is the magnetic field strength in 10^{14} G, P_{ms} is the initial spin period in ms, and the spin-down timescale τ_p is

$$\tau_p = 4.7 B_{14}^{-2} P_{\text{ms}}^2 \text{ days.} \quad (\text{D7})$$

With only magnetar powering, the light-curve parameters are thus τ_m , B_{14} , and P_{ms} . For a given fit to τ_m , the ejecta mass is (from Equation (D2))

$$M_{\text{ej}} = 1 M_{\odot} \times \left(\frac{\tau_m}{10 \text{ days}} \right)^{4/3} \left(\frac{\kappa}{0.1 \text{ cm}^2 \text{ g}^{-1}} \right)^{-2/3} \left(\frac{E_k}{10^{51} \text{ erg}} \right)^{1/3}. \quad (\text{D8})$$

The weak scaling with κ and E_k means that ejecta masses can be meaningfully estimated despite significant uncertainties in κ and E_k .

When the energy input $\int P(t)dt$ approaches or exceeds the explosion energy, accelerations will not be negligible and the homologous approximation becomes poor. A solar mass

of ^{56}Ni emits a total energy of $\int P(t)dt = 1.9 \times 10^{50}$ erg (including the ^{56}Co decay), so for an explosion energy of $\sim 10^{51}$ erg, accelerations will not be important unless $M(^{56}\text{Ni}) \gtrsim 5 M_{\odot}$. A magnetar, on the other hand, has a rotation energy of $2 \times 10^{52} P_{\text{ms}}^{-2}$ erg, so for fast braking with efficient trapping, the ejecta can be accelerated to far beyond its explosive velocities. This is a major limitation of using the homologous expansion approximation, and the consequences for the light curve can only be investigated with numerical radiation hydrodynamics (see Bucciantini et al. 2009 and reference therein for some examples).

D.1. The Opacity

The opacity due to electron scattering is

$$\kappa_{\text{es}} = 0.2 \left(\frac{\bar{Z}/\bar{A}}{0.5} \right) \left(\frac{x_e}{\bar{Z}} \right) \text{ cm}^2 \text{ g}^{-1}, \quad (\text{D9})$$

Table A5
Observed (Non-*K*-corrected) Photometry of SN 2011kf and Associated Errors in Parentheses, Plus Host (See Table A1)

Date	MJD	Phase ^a	<i>g</i>	<i>r</i>	<i>i</i>	<i>z</i>	Telescope
2011 Dec 30	55925.54	0.0	18.60 (0.08)				ATel 3873
2012 Jan 25	55951.54	20.9	19.15 (0.08)				LT
2012 Feb 21	55979.74	43.5	20.91 (0.08)	19.79 (0.06)	19.55 (0.05)	19.40 (0.10)	LT
2012 Feb 22	55980.71	44.3	20.91 (0.11)	19.83 (0.05)	19.52 (0.07)	19.31 (0.10)	LT
2012 Feb 23	55981.62	45.0	20.93 (0.05)				LT
2012 Feb 24	55982.69	45.9	20.96 (0.11)	19.86 (0.06)	19.61 (0.06)	19.41 (0.06)	LT
2012 Mar 8	55995.71	56.4		20.24 (0.08)	19.87 (0.10)	19.64 (0.21)	LT
2012 Mar 10	55997.68	57.9	21.40 (0.19)	20.32 (0.11)	19.95 (0.09)	19.71 (0.19)	LT
2012 Mar 12	55999.69	59.6	21.44 (0.19)	20.39 (0.10)	19.97 (0.08)	19.78 (0.12)	LT
2013 Mar 13	56000.70	60.4	21.45 (0.10)	20.39 (0.05)	19.99 (0.11)	19.81 (0.19)	LT
2012 Mar 18	56005.67	64.4	21.54 (0.09)	20.51 (0.06)	20.13 (0.09)	19.97 (0.10)	LT
2012 Mar 23	56010.65	68.4	21.69 (0.16)	20.80 (0.10)	20.40 (0.15)	20.25 (0.19)	LT
2012 Mar 27	56014.66	71.6	21.95 (0.11)	21.03 (0.12)	20.55 (0.18)	20.52 (0.20)	LT
2012 May 24	56073.15	118.9	23.14 (0.21) ^b	22.07 (0.14) ^b	21.88 (0.13) ^b	21.81 (0.15) ^b	WHT
2012 Jun 27	56106.04	145.4	>23.61	>22.7	>22.2	>22.0	WHT
<i>Host</i>							
2012 Jun 27	56106.04	145.4				>22.0	WHT
2012 Jul 20	56128.94	163.8	24.24 (0.34)	23.94 (0.30)	22.56 (0.33)		WHT
2009 May 6	54987.25		>22.2	>22.2	>21.3	>20.5	SDSS DR9

Notes. LT = 2.0 m Liverpool Telescope +RATCam; WHT = 4.2 m William Herschel Telescope +ACAM.

^a Phase with respect to the *g*-band maximum, corrected for time dilation.

^b Magnitudes after image subtraction using 163 day images and SDSS *griz* images.

Table A6
Observed (Non-*K*-corrected) Photometry of SN 2012il and Associated Errors in Parentheses, Plus Host (see Table A1)

Date	MJD	Phase ^a	<i>g</i>	<i>r</i>	<i>i</i>	<i>z</i>	Telescope
2011 Dec 31	55927.56	-11.8		18.75 (0.09)			CSS
2012 Jan 5	55932.45	-7.6				18.99 (0.03)	PS1
2012 Jan 5	55932.49	-7.6				18.96 (0.03)	PS1
2012 Jan 14	55941.43	0.0		17.98 (0.06)			CSS
2012 Jan 19	55946.44	4.3	18.34 (0.01)				PS1
2012 Jan 21	55948.52	6.0		18.11 (0.07)			CSS
2012 Feb 4	55961.54	17.1			18.94 (0.02)		PS1
2012 Feb 5	55961.55	17.1			18.99 (0.02)		PS1
2012 Feb 11	55969.56	23.9		18.96 (0.10)			CSS
2012 Feb 20	55978.05	31.2	19.83 (0.03)	19.32 (0.09)	19.30 (0.07)	19.45 (0.12)	FTN
2012 Feb 22	55980.56	33.3		19.35 (0.10)			CSS
2012 Feb 23	55981.02	33.7	20.00 (0.05)	19.42 (0.04)			FTN
2012 Feb 29	55987.48	39.2		19.74 (0.14)			CSS
2012 Mar 14	56000.89	50.6	20.97 (0.07)	20.16 (0.07)	20.04 (0.08)	19.85 (0.09)	FTN
2012 Mar 19	56005.86	54.8	21.11 (0.06)	20.25 (0.07)			FTN
2012 Mar 20	56006.90	55.7	21.11 (0.07)	20.26 (0.05)	20.16 (0.05)	20.06 (0.14)	FTN
2012 Apr 23	56009.89	58.3	21.19 ^b (0.08)	20.35 (0.03)			FTN
2012 Mar 24	56010.88	59.1	21.20 ^b (0.09)	20.39 (0.08)	20.28 (0.12)	20.18 (0.09)	FTN
2012 Mar 29	56015.86	63.3	21.29 ^b (0.11)	20.47 (0.07)	20.40 (0.08)	20.30 (0.01)	FTN
2012 May 26	56074.02	113.2		21.23 (0.20) ^b	21.00 (0.22) ^b	20.87 (0.20) ^b	WHT
<i>Host</i>							
2013 Feb 10	56333.04	327.2	22.14 (0.17)	21.57 (0.06)	21.51 (0.08)	21.54 (0.35)	WHT
2005 Feb 3	53405.24		22.13 (0.08)	21.46 (0.07)	21.64 (0.11)	21.50 (0.35)	SDSS DR9

Notes. CSS = 0.7 m Catalina Schmidt Telescope; PS1 = 1.8 m Pan-STARRS1; FTN = 2.0 m Faulkes Telescope North + MEROPE; WHT = 4.2 m William Herschel Telescope + ACAM.

^a Phase with respect to the *g*-band maximum, corrected for time dilation.

^b Magnitudes after image subtraction using 327 day images.

where \bar{Z} is the mean atomic charge, \bar{A} is the mean atomic mass, and $x_e = n_e/n_{\text{nuclei}}$ is the ionization fraction. For any chemical mixture excluding hydrogen, $\bar{Z}/\bar{A} \approx 0.5$, which we can assume since there is no trace of hydrogen lines in the spectra of these objects. The radiation temperature in a radiation-pressure-dominated uniform sphere of internal energy $E(t)$ is

$$\begin{aligned}
 T(t) &= \left(\frac{E(t)}{a \frac{4\pi}{3} V_{\text{ej}}^3 t^3} \right)^{1/4} \\
 &\sim 10^5 \text{ K} \left(\frac{E(t)}{10^{51} \text{ erg}} \right)^{-1/8} \left(\frac{M}{1 M_{\odot}} \right)^{3/8} \left(\frac{t}{10 \text{ days}} \right)^{-3/4}.
 \end{aligned}
 \tag{D10}$$

Table A7
Observed (Non-*K*-corrected) UVOT Ultraviolet AB Magnitudes of SL-SNe Ic Plus Associated Errors in Parentheses

Date	MJD	Phase ^a	<i>uvw</i> 2	<i>uvm</i> 2	<i>uvw</i> 1
PTF10hgi					
2010 Jul 13	55390.31	25.8	21.93 (0.24)	22.05 (0.27)	20.97 (0.22)
2010 Jul 18	55395.50	30.5	22.38 (0.43)	22.40 (0.44)	21.77 (0.29)
SN 2011ke					
2011 May 14	55695.87	8.6	20.67 (0.12)	20.42 (0.13)	18.86 (0.12)
2011 May 30	55711.92	22.6	21.90 (0.21)	21.71 (0.17)	21.09 (0.21)
2011 Jun 6	55718.87	28.7	22.01 (0.37)	21.63 (0.27)	
2011 Jun 7	55719.73	29.6	22.27 (0.41)	22.14 (0.38)	21.53 (0.27)
2011 Jun 8	55720.87	30.5	22.43 (0.48)	22.40 (0.49)	21.67 (0.43)
2012 Mar 8	55994.99	270.3	>23.2	>23.1	>23.3
PTF11rks					
2011 Dec 30	55925.24	-6.2	20.92 (0.12)	21.12 (0.13)	20.42 (0.12)
2012 Jan 1	55927.06	-4.6	21.22 (0.14)	21.52 (0.15)	20.45 (0.14)
2012 Jan 5	55931.35	-0.8	21.47 (0.14)	21.59 (0.15)	21.17 (0.18)
2012 Jan 10	55936.21	3.6	21.54 (0.15)	21.63 (0.20)	21.28 (0.20)
2012 Jan 15	55941.01	7.8	22.00 (0.21)	21.68 (0.26)	21.42 (0.24)
SN 2012il					
2012 Feb 13	55971.71	25.3		22.14 (0.19)	21.33 (0.38)
2012 Feb 14	55971.07	25.6	22.48 (0.26)		21.60 (0.26)

Note. ^a Phases with respect to the *g*-band maxima, corrected for time dilation.

Table A8
Magnitudes of the Local Sequence Stars in the Field of PTF10hgi

ID	<i>g</i>	<i>r</i>	<i>i</i>	<i>z</i>
1	19.52 (0.05)	18.04 (0.03)	17.30 (0.03)	17.00 (0.04)
2	16.80 (0.01)	15.85 (0.02)	15.40 (0.02)	15.23 (0.02)
3	17.44 (0.02)	16.51 (0.02)	16.12 (0.02)	16.00 (0.02)
4	21.27 (0.08)	19.99 (0.05)	19.44 (0.05)	19.13 (0.05)
5	20.16 (0.05)	19.35 (0.05)	19.06 (0.04)	19.02 (0.05)
6	20.60 (0.06)	19.97 (0.05)	19.70 (0.05)	19.56 (0.07)
7	21.34 (0.08)	19.89 (0.05)	18.70 (0.04)	18.24 (0.05)
8	19.29 (0.04)	18.17 (0.04)	17.66 (0.03)	17.50 (0.05)
9	19.64 (0.05)	18.81 (0.04)	18.37 (0.03)	18.30 (0.05)
10	19.26 (0.04)	18.18 (0.04)	17.76 (0.03)	17.60 (0.05)
11	17.94 (0.03)	17.42 (0.03)	17.24 (0.03)	17.20 (0.04)
12	20.21 (0.06)	19.76 (0.05)	19.59 (0.05)	19.61 (0.06)

Note. cf. Figure 15.

In LTE, and at relevant densities here, the ionization fraction of a pure oxygen plasma at $T = 10^5$ K is $x_e \sim 6$, for carbon it is $x_e \sim 4$, and for Fe is $x_e \sim 10$. It should thus be a reasonable approximation to use $x_e/\bar{Z} = 0.5$. With this choice $\kappa_{es} = 0.1 \text{ cm}^2 \text{ g}^{-1}$, comparable to the value $\kappa = 0.08$ that Arnett (1982) uses.

In rapidly expanding media, line opacity can become comparable to or exceed electron scattering opacity (Karp et al. 1977), which complicates analytical light curve modeling. A common simplistic approach to take line opacity into account is to put a minimum value on the opacity. In previous works, values ranging between 0.01 and $0.24 \text{ cm}^2 \text{ g}^{-1}$ have been used (e.g., Herzig et al. 1990; Swartz et al. 1991; Young 2004; Bersten et al. 2011, 2012). The implication of line opacity is that κ is likely to stay in the 0.01 – $0.2 \text{ cm}^2 \text{ g}^{-1}$ range throughout the evolution, and $\kappa = 0.1 \text{ cm}^2 \text{ g}^{-1}$ is probably not off by more than a factor of a few at any given time.

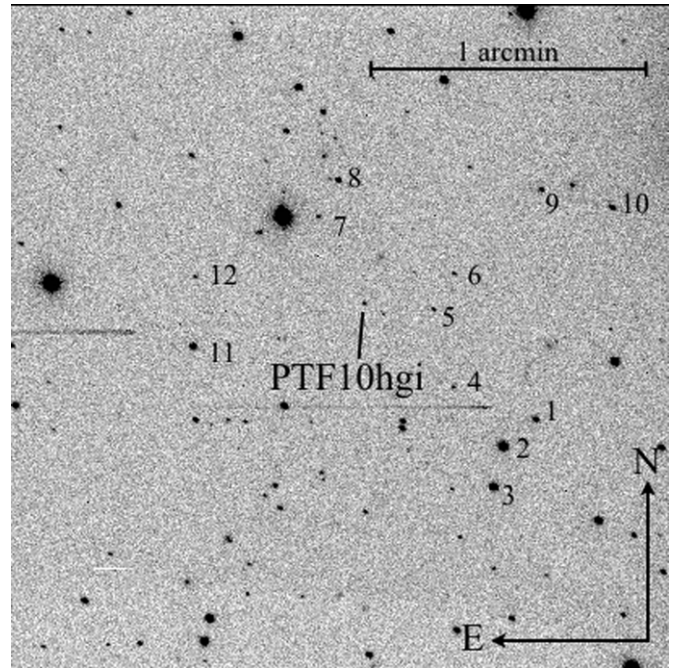


Figure 15. *r*-band image of PTF10hgi obtained with LT + RATCam on 2010 September 5. The sequence of stars used to calibrate the optical magnitudes is indicated by numbers.

D.2. Deposition of Magnetar Radiation

The spectral and directional distribution of the magnetar radiation is highly uncertain. At early times, most radiation will undoubtedly be absorbed, but at later times this is not certain (Kotera et al. 2013). X-rays are efficiently absorbed for a long time by photoionization from inner shell electrons, but gamma-rays see a smaller opacity and start escaping after a few weeks for typical ejecta parameters.

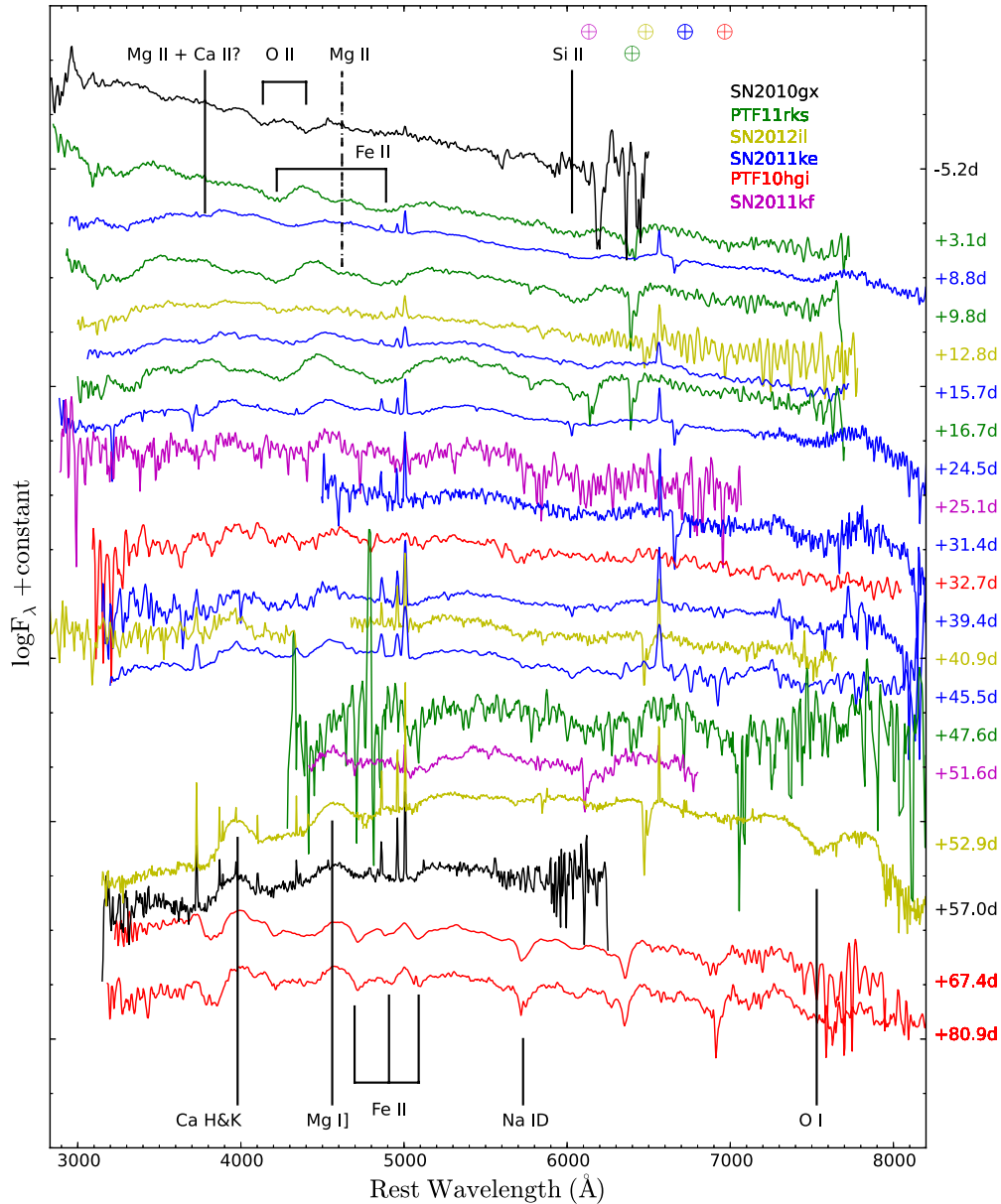


Figure 16. Same as Figure 8, but with all the spectra convolved with a factor of five and subsequently binned to a 5 \AA scale. Spectra of PTF11rks are in green, SN 2011ke in blue, SN 2012il in gold, PTF10hgi in red, SN 2011kf in magenta, and SN 2010gx (Pastorello et al. 2010) in black. The phase of each spectrum relative to light curve peak in the rest frame is shown on the right. The spectra are corrected for extinction and reported in their rest frame. The most prominent features are labeled.

(A color version of this figure is available in the online journal.)

Here, we assume full trapping of the magnetar radiation. Most of the energy input occurs over a few weeks after explosion, and it is a reasonable assumption that most of the energy emerges as X-rays, as in the Crab pulsar, for instance (Weisskopf et al. 2000).

D.3. Photospheric Velocities and Temperatures

To estimate the photospheric velocities and temperatures for a given solution for ejecta mass, we approximate the ejecta density structure with a core + envelope morphology. The velocity of the homogenous core (which contains almost all the mass to force consistency with the diffusion calculation) is determined from

$$\frac{3}{10} M_{\text{ej}} V_{\text{core}}^2 = E_{\text{k}} \quad (\text{D11})$$

and its density is given by

$$\rho_{\text{core}}(t) = \frac{M_{\text{ej}}}{\frac{4\pi}{3} V_{\text{core}}^3 t^3}. \quad (\text{D12})$$

Outside we attach an envelope with density profile

$$\rho(t, V) = \rho_{\text{core}}(t) \left(\frac{V}{V_{\text{core}}} \right)^{-\alpha}. \quad (\text{D13})$$

The optical depth of the envelope is

$$\tau_{\text{env}} = \int_{R_{\text{core}}}^{\infty} \rho_{\text{core}} \left(\frac{r}{R_{\text{core}}} \right)^{-\alpha} \kappa dr \quad (\text{D14})$$

$$= \frac{\rho_{\text{core}} R_{\text{core}} \kappa}{\alpha - 1} \quad (\text{D15})$$

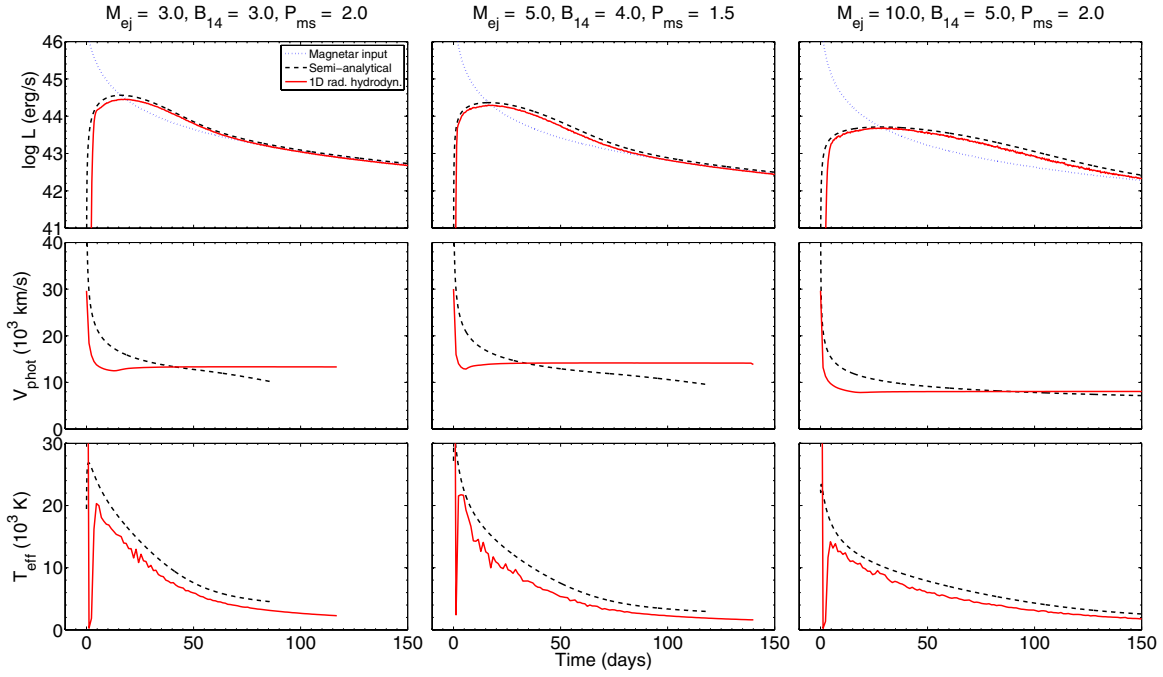


Figure 17. Comparison of light curves, photospheric velocities, and photospheric temperatures from our semi-analytical model (black dashed) and the one-dimensional radiation hydrodynamical simulations of Kasen & Bildsten (2010, red solid). Also shown is the input magnetar energy (blue dotted line).

(A color version of this figure is available in the online journal.)

Table A9

Best-fitting Values of System Parameters (After the Slash) Compared to the Actual Simulation Values of Kasen & Bildsten (2010, Before the Slash); Derived Parameters on the Right

M_{ej}	B_{14}	P_{ms}	Shift (days)	E^{mag}
3.0/3.0	2.0/2.2	2.0/2.3	-1.57/0	3.9
3.0/3.1	3.0/3.2	2.0/2.3	0.17/0	4.0
3.0/2.8	5.0/5.4	2.0/2.4	-0.038/0	3.6
5.0/3.1	3.0/3.2	2.0/2.3	0.18/0	3.9
5.0/3.0	4.0/4.3	2.0/2.4	7e-4/0	3.7
5.0/3.0	5.0/5.4	2.0/2.4	0.18/0	3.7
7.0/4.1	2.0/2.1	1.5/1.8	-0.039/0	6.6
7.0/3.8	3.0/3.2	1.5/1.9	-4.9e-4/0	6.1
10/12.8	2.0/2.7	2.0/1.6	-5.0/0	8.0
10/9.2	3.0/3.5	2.0/2.2	-3.6/0	4.3
10/7.4	5.0/5.1	2.0/2.9	1.8e-4/0	2.4

$$= \frac{\tau_{core}}{\alpha - 1}, \quad (D16)$$

where

$$\tau_{core}(t) = \kappa \rho_{core}(t) V_{core} t. \quad (D17)$$

One should in general distinguish between the photosphere and the thermalization layer, where the temperature of the continuum is determined. The position of these depends on the total opacity κ and the absorption opacity κ_a , respectively. However, due to our simple treatment such detail is unwarranted, and we approximate them to be the same, R_* . As long as the atmosphere is optically thick ($\tau_{env} > 1$), $R_*(t)$ is found from solving

$$\int_{R_*(t)}^{\infty} \kappa \rho(r, t) dr = 1, \quad (D18)$$

Table A10

Best-fit Parameters for ^{56}Ni Modeling of the Bolometric Light Curves and χ^2_{red}

Object	Shift (day)	$M(^{56}\text{Ni})$ (M_{\odot})	M_{ej} (M_{\odot})	E (10^{51} erg)	t_0 (MJD)	χ^2_{red}
SN 2011ke	36.0	3.0	6.1	8.1	55650.65	35
SN 2011kf	38.0	5.0	11	15.0	55920.65	58
SN 2012il	26.0	2.9	5.9	6.2	55918.56	193
PTF10hgi	37.0	2.6	5.9	6.2	55322.78	1.2
PTF11rks	31.0	3.0	6.1	8.1	55912.11	53
SN 2010gx	30.0	6.0	13.0	15.0	55269.22	860

which gives

$$R_*(t) = R_{core}(t) \left(\frac{\alpha - 1}{\tau_{core}(t)} \right)^{\frac{1}{1-\alpha}}. \quad (D19)$$

If the photosphere has receded into the core, the expression is instead

$$R_*(t) = R_{core}(t) - \frac{1 - \frac{\tau_{core}}{\alpha - 1}}{\kappa \rho_{core}}. \quad (D20)$$

Typical density profiles in Ib/c models show $\alpha \sim 10$ (e.g., Figure 1 in Kasen & Bildsten 2010), which is the value we use here.

From the photospheric radius $R_*(t)$ we retrieved the velocity at the photosphere (V_{phot})

$$V_{phot}(t) = V_{core} \frac{R_*(t)}{R_{core}(t)}. \quad (D21)$$

The effective temperature is found from application of the blackbody formula, using the model luminosities at corresponding times.

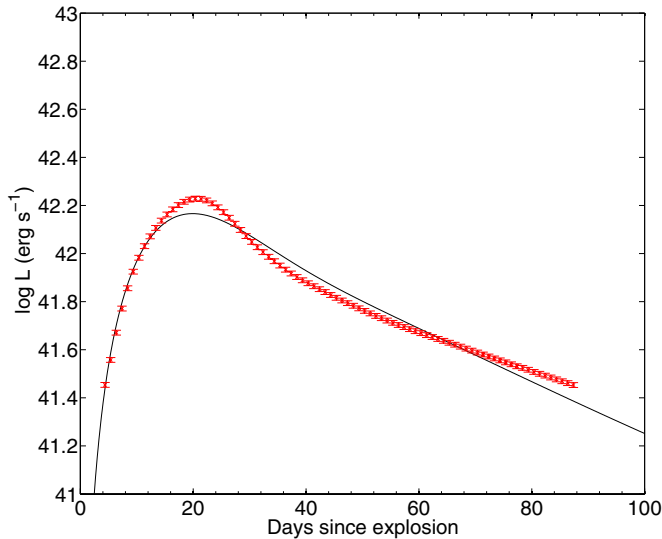


Figure 18. Fit to the bolometric light curve of SN 2011dh (Ergon et al. 2013). The fit values are $M_{\text{ej}} = 2.2 M_{\odot}$ and $M_{56\text{Ni}} = 0.08 M_{\odot}$, for $E_k = 10^{51}$ erg and $\kappa = 0.1 \text{ cm}^2 \text{ g}^{-1}$.

(A color version of this figure is available in the online journal.)

D.4. Additional Tests

To test the applicability of our approach, we perform three tests. The first one is to compare light curves, photospheric velocities, and temperatures to the radiation hydrodynamical simulations of Kasen & Bildsten (2010). Figure 17 shows three representative examples. For these comparisons, we use Equation (3) to relate magnetar energy to ejecta kinetic energy, which shows itself a good approximation. Table A9 shows the derived parameters of M_{ej} , B_{14} , P_{ms} , and Δt for a series of simulations in Kasen & Bildsten (2010). The magnetar properties (B_{14} and P_{ms}) are reliably recovered to within 10%–20% of their input values, whereas the ejecta mass can vary, tending to be too low in the fits. It is, however, always within a factor two of the correct value.

The second test is to derive parameters for the Type IIb SN 2011dh, using the approach described above (fixing $E_k = 10^{51}$ erg, $\kappa = 0.1$, $\alpha = 10$). The best fit is shown in Figure 18. The recovered values $M_{\text{ej}} = 2.2 M_{\odot}$ and $M_{56\text{Ni}} = 0.08 M_{\odot}$ agree well with the results from Bersten et al. (2011), who used radiation hydrodynamical simulations.

While for the third one, we tried to test our code on Type Ic SNe 1998bw (Galama et al. 1998; McKenzie & Schaefer 1999; Sollerman et al. 2000; Patat et al. 2001) and 2007gr (Valenti et al. 2008; Hunter et al. 2009) to explore its limits. We fitted the first 200 days with the magnetar model (fixing $E_k = 10^{51}$ erg, $\kappa = 0.1$, $\alpha = 10$), recovering $M_{\text{ej}} = 1.8 M_{\odot}$ and $B_{14} = 9.8$ G and $P_{\text{ms}} = 18.9$ ms for SN 1998bw and $M_{\text{ej}} = 1.3 M_{\odot}$ and $B_{14} = 22.9$ G and $P_{\text{ms}} = 47.6$ ms for SN 2007gr. Instead, trying to fit the entire data set, we recover $M_{\text{ej}} = 19.9 M_{\odot}$ and $B_{14} = 16.6$ G and $P_{\text{ms}} = 0.5$ ms for SN 1998bw and $M_{\text{ej}} = 2.5 M_{\odot}$ and $B_{14} = 26.0$ G and $P_{\text{ms}} = 42.6$ ms for SN 2007gr. The best fit to those data are shown in Figure 19 along with the fit of the radioactive decay. The applicability of the Arnett model to derive parameters for radioactivity-driven SNe has also been demonstrated by Valenti et al. (2011). The results imply that at those energies the magnetar contribution is more important after 150–200 days, highlighting the importance of obtaining late-time data.

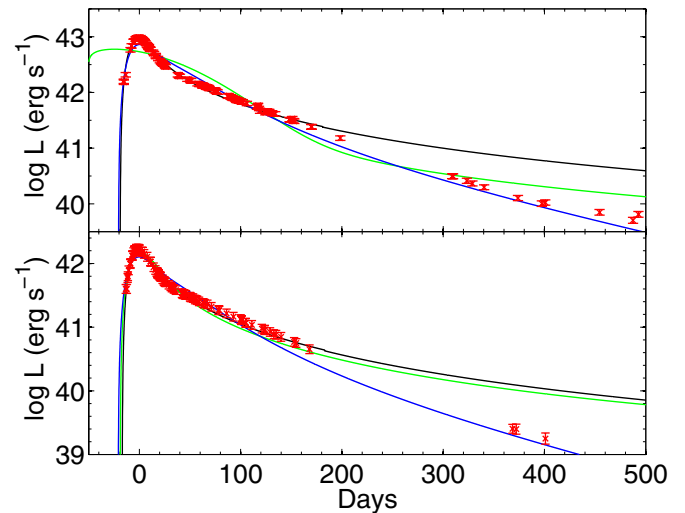


Figure 19. Fit to the bolometric light curve of SNe 1998bw (top) and 2007gr (bottom). Magnetar fit of the first 200 days is shown (black) along with the fit of the entire set (green) and the fit of radioactive decay (blue). Both models can fit the first 50–100 days but are clearly differentiated at late times.

(A color version of this figure is available in the online journal.)

D.5. ^{56}Ni Fits Parameters

For the ^{56}Ni models we computed γ -ray trapping as in Arnett (1982). The parameters are reported in Table A10.

REFERENCES

- Abazajian, K. N., Adelman-McCarthy, J. K., Agüeros, M. A., et al. 2009, *ApJS*, **182**, 543
- Agnoletto, I., Benetti, S., Cappellaro, E., et al. 2009, *ApJ*, **691**, 1348
- Ahn, C. P., Alexandroff, R., Allende Prieto, C., et al. 2012, *ApJS*, **203**, 21
- Alard, C. 2000, *A&AS*, **144**, 363
- Arnett, W. D. 1982, *ApJ*, **253**, 785
- Barbary, K., Dawson, K. S., Tokita, K., et al. 2009, *ApJ*, **690**, 1358
- Barkov, M. V., & Komissarov, S. S. 2011, *MNRAS*, **415**, 944
- Baron, E., Hauschildt, P. H., Branch, D., Kirshner, R. P., & Filippenko, A. V. 1996, *MNRAS*, **279**, 799
- Berger, E., Chornock, R., Lunnan, R., et al. 2012, *ApJL*, **755**, L29
- Bersten, M. C., Benvenuto, O., & Hamuy, M. 2011, *ApJ*, **729**, 61
- Bersten, M. C., Benvenuto, O. G., Nomoto, K., et al. 2012, *ApJ*, **757**, 31
- Blinnikov, S. I., & Sorokina, E. I. 2010, arXiv:1009.4353
- Botticella, M. T., Trundle, C., Pastorello, A., et al. 2010, *ApJL*, **717**, L52
- Bouchet, P., Slezak, E., Le Bertre, T., Moneti, A., & Manfroid, J. 1989, *A&AS*, **80**, 379
- Bucciantini, N., Quataert, E., Metzger, B. D., et al. 2009, *MNRAS*, **396**, 2038
- Cappellaro, E., Mazzali, P. A., Benetti, S., et al. 1997, *A&A*, **328**, 203
- Chandrasekhar, S., & Fermi, E. 1953, *ApJ*, **118**, 116
- Chatzopoulos, E., & Wheeler, J. C. 2012, *ApJ*, **760**, 154
- Chatzopoulos, E., Wheeler, J. C., & Vinko, J. 2009, *ApJ*, **704**, 1251
- Chatzopoulos, E., Wheeler, J. C., & Vinko, J. 2012, *ApJ*, **746**, 121
- Chen, T.-W., Smartt, S. J., Bresolin, F., et al. 2013, *ApJL*, **763**, L28
- Chevalier, R. A., & Irwin, C. M. 2011, *ApJL*, **729**, L6
- Chomiuk, L., Chornock, R., Soderberg, A. M., et al. 2011, *ApJ*, **743**, 114
- Chomiuk, L., Soderberg, A., Margutti, R., et al. 2012, *ATel*, **3931**, 1
- Dessart, L., Hillier, D. J., Waldman, R., Livne, E., & Blondin, S. 2012, *MNRAS*, **426**, L76
- Dexter, J., & Kasen, D. 2012, arXiv:1210.7240
- Drake, A. J., Djorgovski, S. G., Mahabal, A., et al. 2009, *ApJ*, **696**, 870
- Drake, A. J., Djorgovski, S. G., Mahabal, A. A., et al. 2011, *ATel*, **3343**, 1
- Drake, A. J., Djorgovski, S. G., Mahabal, A. A., et al. 2012, *ATel*, **3873**, 1
- Drout, M. R., Soderberg, A. M., Gal-Yam, A., et al. 2011, *ApJ*, **741**, 97
- Duncan, R. C., & Thompson, C. 1992, *ApJL*, **392**, L9
- Eldridge, J. J., Fraser, M., Smartt, S. J., Maund, J. R., & Crockett, R. M. 2013, arXiv:1301.1975
- Ensmann, L. M., & Woosley, S. E. 1988, *ApJ*, **333**, 754
- Ergon, M., Sollerman, J., Fraser, M., et al. 2013, arXiv:1305.1851
- Galama, T. J., Vreeswijk, P. M., van Paradijs, J., et al. 1998, *Natur*, **395**, 670

- Gal-Yam, A. 2012, *Sci*, **337**, 927
- Gal-Yam, A., Mazzali, P., Ofek, E. O., et al. 2009, *Natur*, **462**, 624
- Gezari, S., Chornock, R., Rest, A., et al. 2012, *Natur*, **485**, 217
- Gezari, S., Halpern, J. P., Grupe, D., et al. 2009, *ApJ*, **690**, 1313
- Ginzburg, S., & Balberg, S. 2012, *ApJ*, **757**, 178
- Hadjjyska, E., Rabinowitz, D., Baltay, C., et al. 2012, in IAU Symp. 285, New Horizons in Time-domain Astronomy, ed. E. Griffin, R. Hanison, & R. Seaman (Cambridge: Cambridge Univ. Press), 324
- Hamuy, M. 2003, *ApJ*, **582**, 905
- Hamuy, M., Suntzeff, N. B., Gonzalez, R., & Martin, G. 1988, *AJ*, **95**, 63
- Herzig, K., El Eid, M. F., Fricke, K. J., & Langer, N. 1990, *A&A*, **233**, 462
- Hodapp, K. W., Siegmund, W. A., Kaiser, N., et al. 2004, *Proc. SPIE*, **5489**, 667
- Hunter, D. J., Valenti, S., Kotak, R., et al. 2009, *A&A*, **508**, 371
- Kaiser, N., Burgett, W., Chambers, K., et al. 2010, *Proc. SPIE*, **7733**, 12K
- Karp, A. H., Lasher, G., Chan, K. L., & Salpeter, E. E. 1977, *ApJ*, **214**, 161
- Kasen, D., & Bildsten, L. 2010, *ApJ*, **717**, 245
- Kotera, K., Phinney, E. S., & Olinto, A. V. 2013, *MNRAS*, in press (arXiv:1304.5326)
- Leloudas, G., Chatzopoulos, E., Dilday, B., et al. 2012, *A&A*, **541**, A129
- Magnier, E. 2007, in ASP Conf. Ser. 364, The Future of Photometric, Spectrophotometric and Polarimetric Standardization, ed. C. Sterken (San Francisco, CA: ASP), 153
- Magnier, E. A., Liu, M., Monet, D. G., & Chambers, K. C. 2008, in IAU Symp. 248, A Giant Step: From Milli- to Micro-arcsecond Astrometry, ed. W. J. Jin, I. Platais, & M. A. C. Perryman (Cambridge: Cambridge Univ. Press), 553
- Magnier, E. A., Schlafly, E., Finkbeiner, D., et al. 2013, *ApJS*, **205**, 20
- Mahabal, A. A., & Drake, A. J. 2010, *ATel*, **2508**, 1
- Margutti, R., Soderberg, A., Chomiuk, L., et al. 2012, *ATel*, **3925**, 1
- McKenzie, E. H., & Schaefer, B. E. 1999, *PASP*, **111**, 964
- Meynet, G., Eggenberger, P., & Maeder, A. 2011, *A&A*, **525**, L11
- Moriya, T. J., & Tominaga, N. 2012, *ApJ*, **747**, 118
- Neill, J. D., Sullivan, M., Gal-Yam, A., et al. 2011, *ApJ*, **727**, 15
- Ofek, E. O., Cameron, P. B., Kasliwal, M. M., et al. 2007, *ApJL*, **659**, L13
- Ostriker, J. P., & Gunn, J. E. 1971, *ApJL*, **164**, L95
- Pastorello, A., Smartt, S. J., Botticella, M. T., et al. 2010, *ApJL*, **724**, L16
- Patat, F., Cappellaro, E., Danziger, J., et al. 2001, *ApJ*, **555**, 900
- Poole, T. S., Breeveld, A. A., Page, M. J., et al. 2008, *MNRAS*, **383**, 627
- Prieto, J. L., Drake, A. J., Mahabal, A. A., et al. 2012, *ATel*, **3883**, 1
- Quimby, R. M., Aldering, G., Wheeler, J. C., et al. 2007, *ApJL*, **668**, L99
- Quimby, R. M., Castro, F., Gerardy, C. L., et al. 2005, *BAAS*, **207**, 171.02
- Quimby, R. M., Gal-Yam, A., Arcavi, I., et al. 2011a, *ATel*, **3841**, 1
- Quimby, R. M., Kulkarni, S., Ofek, E., et al. 2010, *ATel*, **2740**, 1
- Quimby, R. M., Kulkarni, S. R., Kasliwal, M. M., et al. 2011b, *Natur*, **474**, 487
- Quimby, R. M., Sternberg, A., & Matheson, T. 2011c, *ATel*, **3344**, 1
- Rau, A., Kulkarni, S. R., Law, N. M., et al. 2009, *PASP*, **121**, 1334
- Schlegel, D. J., Finkbeiner, D. P., & Davis, M. 1998, *ApJ*, **500**, 525
- Shigeyama, T., Nomoto, K., Tsujimoto, T., & Hashimoto, M.-A. 1990, *ApJL*, **361**, L23
- Smartt, S. J., Valenti, S., Magill, L., et al. 2011, *ATel*, **3351**, 1
- Smartt, S. J., Wright, D., Valenti, S., et al. 2012, *ATel*, **3918**, 1
- Smith, N., Li, W., Foley, R. J., et al. 2007, *ApJ*, **666**, 1116
- Smith, N., & McCray, R. 2007, *ApJL*, **671**, L17
- Sollerman, J., Kozma, C., Fransson, C., et al. 2000, *ApJL*, **537**, L127
- Swartz, D. A., Wheeler, J. C., & Harkness, R. P. 1991, *ApJ*, **374**, 266
- Taubenberger, S., Pastorello, A., Mazzali, P. A., et al. 2006, *MNRAS*, **371**, 1459
- Thompson, T. A., Chang, P., & Quataert, E. 2004, *ApJ*, **611**, 380
- Tonry, J., & Onaka, P. 2009, in Proc. Advanced Maui Optical and Space Surveillance Technologies Conf., ed. S. Ryan, E40
- Tonry, J. L., Stubbs, C. W., Kilic, M., et al. 2012a, *ApJ*, **745**, 42
- Tonry, J. L., Stubbs, C. W., Lykke, K. R., et al. 2012b, *ApJ*, **750**, 99
- Umeda, H., & Nomoto, K. 2008, *ApJ*, **673**, 1014
- Usov, V. V. 1992, *Natur*, **357**, 472
- Valenti, S., Elias-Rosa, N., Taubenberger, S., et al. 2008, *ApJL*, **673**, L155
- Valenti, S., Fraser, M., Benetti, S., et al. 2011, *MNRAS*, **416**, 3138
- Valenti, S., Smartt, S., Young, D., et al. 2010, *ATel*, **2773**, 1
- Weisskopf, M. C., Hester, J. J., Tennant, A. F., et al. 2000, *ApJL*, **536**, L81
- Wheeler, J. C., Yi, I., Höflich, P., & Wang, L. 2000, *ApJ*, **537**, 810
- Woods, P. M., & Thompson, C. 2006, in Compact Stellar X-Ray Sources, ed. W. Lewin & M. van der Klis (Cambridge Astrophysics Series, No. 39; Cambridge: Cambridge Univ. Press), 547
- Woosley, S. E. 2010, *ApJL*, **719**, L204
- Woosley, S. E., Blinnikov, S., & Heger, A. 2007, *Natur*, **450**, 390
- Woosley, S. E., Hartmann, D., & Pinto, P. A. 1989, *ApJ*, **346**, 395
- York, D. G., Adelman, J., Anderson, J. E., Jr., et al. 2000, *AJ*, **120**, 1579
- Young, D. R., Smartt, S. J., Valenti, S., et al. 2010, *A&A*, **512**, A70
- Young, T. R. 2004, *ApJ*, **617**, 1233